Qeios

Research Article

Outer Solar System Spacecraft Without Drag-Free Control to Probe the µHz Gravitational Wave Frontier

Matthew McQuinn[1], Casey McGrath[2,3,4]

1. Department of Astronomy, University of Washington, United States; 2. Center for Space Sciences and Technology, University of Maryland, Baltimore County, United States; 3. Gravitational Astrophysics Lab, Goddard Space Flight Center, Greenbelt, United States; 4. Center for Research and Exploration in Space Science and Technology II, Goddard Space Flight Center, Greenbelt, United States

The microhertz frequency band of gravitational waves probes the merger of supermassive black holes as well as many other gravitational wave phenomena. However, space-interferometry methods that use test masses would require substantial development of test-mass isolation systems to detect anticipated astrophysical events. We propose an approach that avoids on-board inertial test masses by situating spacecraft in the low-acceleration environment of the outer Solar System. We show that for Earth-spacecraft and inter-spacecraft distances of $\gtrsim 10$AU, the accelerations on the spacecraft would be sufficiently small to potentially achieve gravitational wave sensitivities determined by stochastic gravitational wave backgrounds. We further argue, for arm lengths of $10 - 30$AU and ~ 10Watt transmissions, that stable phase locks could be achieved with 20cm mirrors or 5m radio dishes, although for the laser case this would require lower laser frequency noise relative to the LISA lasers. We discuss designs that send both laser beams and radio waves between the spacecraft, finding that despite the $\sim 10^4 \times$ longer wavelengths, even a design with radio transmissions could reach stochastic background-limited sensitivities at $\lesssim 0.3 \times 10^{-4}$ Hz. Operating in the radio significantly reduces many spacecraft design tolerances. Our baseline concept requires two arms to do interferometry. However, if one spacecraft carries a clock with Allan deviations at 10^4 seconds of 10^{-17}, a comparable sensitivity could be achieved with a single arm. Finally, we discuss the feasibility of achieving similar gravitational wave sensitivities in a 'Doppler tracking' configuration where the single arm is anchored to Earth.

Corresponding author: Matthew McQuinn, mcquinn@uw.edu

1. Introduction

It has been less than a decade since the first direct detection of gravitational waves by the LIGO/Virgo collaboration[1]. In subsequent years, the LIGO/Virgo collaboration has cataloged more than a hundred black hole merger events at kilohertz frequencies[2], as well as several neutron star merger candidates, including the famous 2017 multi-messenger event[3]. Recently, the observed spectral range of gravitational waves has been extended to almost a nanohertz with the likely detection of a stochastic gravitational wave background using pulsar timing arrays[4][5][6], a signal that probably owes to the inspirals of the most massive supermassive black hole binaries.

A gravitational wave interferometer sensitive to significantly lower frequencies than LIGO/Virgo requires going to outer space because of seismic noise as well as other terrestrial noise sources. The Laser Interferometer Space Antenna (LISA), scheduled for launch starting in 2035[7], aims to fill in the $10^{-4} - 1 \mathrm{Hz}$ waveband that is intermediate between the pulsar timing arrays and the ground-based efforts like LIGO/Virgo. LISA will send laser beams between three spacecraft in a triangle configuration with side lengths of 0.017AU. The lasers will work as multiple Michelson-like interferometers, with the aim of measuring phase changes that result from displacements as small as an angstrom. The reference for these precise displacement measurements must be sufficiently isolated from sources of acceleration (such as the Sun's irradiance variations) to reach the sensitivities needed to detect known astrophysical gravitational wave sources. Each LISA spacecraft employs the most sensitive accelerometer ever built, which works by monitoring a nearly drag-free test mass.

Considerable effort has been directed towards finding detection strategies in other regions of the gravitational wave spectrum. The most exciting frontiers are the decihertz region, between the waveband probed by LISA and LIGO/Virgo[8], and the "microhertz" band of $10^{-7} - 10^{-4}$ Hz, which falls between the pulsar timing arrays and LISA. This $10^{-7} - 10^{-4}$ Hz band probes the early inspiral of the $\sim 10^5 - 10^{6.5} M_\odot$ black holes that LISA observes nearer to merger, as well as the inspiral and merger of $10^{6.5} - 10^{10} M_\odot$ black holes – the class of black holes that are associated with quasars and may be more likely to yield an electromagnetic counterpart. There are a host of other astrophysical sources that fall in the $10^{-7} - 10^{-4}$ Hz band e.g.[9]. While many proposed methods in this waveband lack sufficient sensitivity for known astrophysical processes, they may still detect larger backgrounds, such as those produced in the early universe[10][11]. One idea is to use measurements of the lunar orbit

by future laser ranging[12]. Another is to use the very precise angular localizations of stars to constrain angular variations from passing gravitational waves, i.e. gravitational wave astrometry[13][14][15]. The proposals forecast to be the most sensitive follow in the spirit of an expanded LISA, where the three spacecraft are situated in an equilateral triangle tracing Earth's orbit[16][17]. Two recent examples are the μAres and LISAmax concepts[9][18].

The μAres concept assumes acceleration isolation to 10^{-15} m s^{-2} Hz$^{-1/2}$ over its proposed frequency band of $10^{-7} - 1$ Hz, which contrasts with the LISA acceleration allowance of 10^{-14} m s^{-2} Hz$^{-1/2}$ at the bottom of the LISA band of 10^{-4} Hz[7]. LISAmax more conservatively takes the same acceleration control specifications as the LISA mission, allowing it to achieve $100\times$ improved sensitivity over LISA owing to the longer arms. LISAmax additionally extrapolates the LISA acceleration control below the LISA band to 1μ Hz assuming the square root of its error power spectrum scales as f^{-2}[18]. However, there are some acceleration sources for the LISA accelerometer that become important at $\sim 2 \times 10^{-5}$ Hz and that scale much more strongly than f^{-2} to lower frequencies, such as thermal-mechanical noise e.g.[19]. Concerned that substantial development in acceleration control would be required for space-interferometers to probe the μ Hz band,[20] considered the possibility of instead establishing stations on two asteroids with orbits around 1 AU and carefully measuring their relative distance. Because of their large masses, the asteroids would behave as excellent test masses, avoiding the need for precise acceleration control.

Here we consider another method to avoid on-board acceleration monitoring – employing spacecraft further out in the Solar System, reaching distances and inter-spacecraft separations of tens of astronomical units. Abandoning drag-free control was considered by[21] and[16] in the context of a LISA-like mission. The outer Solar System application we consider results in a potentially massive reduction in acceleration sources, as the solar irradiance variations and the solar wind density fall off as r^{-2} with distance from the Sun. Arms over which the gravitational wave signal is measured can be oriented perpendicular to the spacecraft-Sun direction to further suppress these largely radial accelerations[21]. Finally, the longer baselines of our outer Solar System concept may relax other system specifications: When fixing the strain noise power due to shot noise at long wavelengths, the timing error, displacement error, and square of the angular pointing error are relaxed in proportion to the baseline distance.

A drawback of such long baselines is that the electromagnetic transmissions between spacecraft would be weak. However, we argue that even for spacecraft that are separated by several tens of astronomical units, Watt-scale electromagnetic transmissions are still sufficiently strong to achieve a stable phase lock. Another concern is that only meager ~ 10kbps downlinks have been achieved to spacecraft in the outer Solar System. Fortunately, only a single phase measurement for every hour of data may be required because of the low frequencies of interest such that an hour per month of ~ 10kbps downlinks would likely be sufficient.

This paper also considers an additional optimization, using radio dishes rather than lasers to measure spacecraft separations. One difficulty with using lasers pertains to the spacecraft relative velocities: larger relative velocities mean larger differences in the interfering frequencies, Δf. As phase errors scale with timing errors δt as $\delta\phi \sim \Delta f \delta t$, many of the spacecraft design tolerances would be set by the magnitude of this frequency difference. While the changes in velocity may be slow enough that small frequency differentials can be achieved by periodically tuning the frequencies with small adjustments to the laser cavity properties, the radio avoids this difficulty by directly measuring the phase of the inter-arm transmissions. Other advantages of the radio include being insensitive to intensity variations in the transmission as well as relaxed pointing requirements. However, using radio broadcasts rather than lasers is potentially much less sensitive to gravitational waves due to the $\sim 10^4$ times longer wavelengths. We show that a radio instrument can still be sufficiently sensitive that acceleration noise (which is insensitive to the transmission wavelength) is dominant over much of the gravitational waveband of interest. Another concern with a radio effort is that plasma dispersion would contaminate the measured phases. We show that this noise can be essentially eliminated using two frequency channels and at only moderate cost to the sensitivity.

A radio design may be more easily added to other outer Solar System spacecraft, which often already include a relatively large high-gain antenna for telemetry.[1]

Indeed, there is a long history of using radio broadcasts to track spacecraft velocities and probe gravitational waves for a review see[22]. There has been recent interest in Doppler tracking in the context of a future outer Solar System mission, where it has been suggested that a large improvement in sensitivity may be possible, pushing Doppler tracking into a regime where it can detect anticipated astrophysical sources[23]. We show that reaching the sensitivity benchmarks in[23] at $f \lesssim 10^{-6}$ Hz would likely require on-board instrumentation that corrects for the accelerations from solar radiation and the interplanetary plasma.

This paper is organized as follows. Section 2 discusses the radiometer and acceleration noise sources that are likely to shape the sensitivity of the proposed concept. Section 3 uses these estimates to predict the concept's gravitational wave sensitivity, where we consider the three general mission architectures illustrated in Figure 1. Section 4 elaborates on some of the instrumental considerations that are most relevant. The appendices discuss the effects of the interplanetary plasma on the phase timing of radio waves, considering dispersion (A) and refraction (B), and also consider the downlink data rates that the concept would require (C).
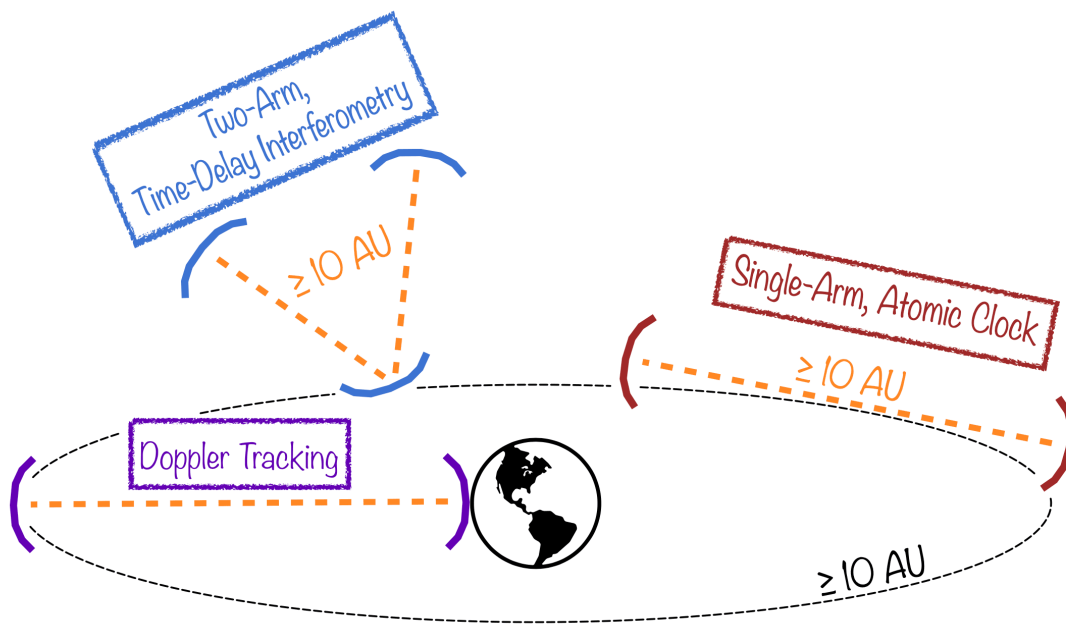
Figure 1. Illustration of the three different architectures considered in this paper: (1) A two-arm design that relies on time-delay interferometry in blue, (2) a single-arm design that relies on a precise atomic clock in red, and (3) an Earth-anchored Doppler tracking design in purple. Our primary focus is on the two-arm time-delay interferometry concept, but we discuss the clock requirements to achieve a comparable sensitivity with a single arm. We contrast the sensitivity of these two designs with the traditional Doppler tracking to outer Solar System spacecraft in § 3.3. For the calculations in this paper, we consider designs with spacecraft-spacecraft and spacecraft-Earth separations of 10 AU and 30 AU, although the spacecraft would be most easily placed on trajectories where they drift outward rather than orbit the Sun (so that their separations would gradually increase with time). As a conceptual reference comparison, Saturn orbits between approximately 9-10 AU, Uranus between approximately 18-20 AU, and Pluto between approximately 30-50 AU.

Unless stated otherwise, 1D power spectra are always half-bandwidth power spectra. As both electromagnetic and gravitational signal frequencies appear in our calculations, to distinguish them, we generally use wavelengths when referring to electromagnetic transmissions that are sent along arms, and we generally use frequencies when referring to gravitational wave signals and their potential noise sources, noting the few cases where we do not. We use Gaussian conventions for electromagnetic quantities such as electron charge (although we do use volt rather than statvolt when referring to spacecraft voltages).

2. Strain noise sources

This section considers the different noise sources that set the sensitivity. We first consider clock errors and their avoidance through time-delay interferometry (§ 2.1), then discuss errors related to the strength of the electromagnetic beams (§ 2.2), and finally discuss acceleration errors (§ 2.3). These noise sources are then used to calculate the gravitational wave sensitivity of our concepts in § 3.

2.1. Clock noise and its mitigation

Single-arm and an atomic clock

Let us first consider a one-arm configuration in which a monochromatic light wave with phase $\phi_{\rm os}$ tied to a on-board oscillator or atomic clock. This wave is sent from one spacecraft to another a distance L_1 away and then returns. If the phase of the incoming signal is compared with the phase on board, up to an overall constant the phase difference is given by e.g. [24]

$$\phi_1 = \phi_{\rm os}(t - 2L_1/c) - \phi_{\rm os}(t) + \frac{2\pi}{\lambda} L_1 h_1(t) + \phi_{1,N}, \tag{1}$$

where $2\pi c/\lambda$ is the electromagnetic wave's angular frequency, $\phi_{1,N}$ is the noise, and $\frac{2\pi}{\lambda} \times L_1 h_1(t)$ is the gravitational wave contribution to the phase in the long wavelength limit $c/f \gg L_1$. (This limit applies at our target of 1μHz, where the gravitational wavelength is 2000~AU.) The phase of the electromagnetic signal $\phi_{\rm os}$ has noise that can be related to the Allan deviation $\sigma_y(\tau)$ of the clock. If we assume that the clock's frequency noise is white such that $\sigma_y(\tau)^2 \propto \tau^{-1}$, the phase noise power is [25]

$$S_{\rm os}(f) \equiv 2T^{-1}\langle \tilde{\phi}_{\rm os}^2 \rangle = \frac{2(2\pi c/\lambda)^2 \times \tau \times \sigma_y(\tau)^2}{(2\pi f)^2}, \tag{2}$$

where $\tilde{\phi}_{os}$ is the Fourier transform of $\phi_{os}(t)$ over time interval T. Since the phase difference given by equation (1) involves ϕ_{os} at two times, the phase noise power relevant for constraining h_1 is

$$S_{os,tot} = 2S_{os}\left[1 - \cos(4\pi L_1 f/c)\right].\tag{3}$$

Equation (3) allows us to calculate the long-wavelength strain noise power of our interferometer owing to white frequency modulation clock noise:

$$\tilde{h}_{os}^{LW} = \frac{\sqrt{S_{os,tot}}}{(2\pi/\lambda)L_1} = 2^{3/2}(1s)^{1/2} \times \sigma_y(1s) = 2.8 \times 10^{-13}\mathrm{Hz}^{-1/2}\left(\frac{\sigma_y(1s)}{10^{-13}}\right).\tag{4}$$

where we have adopted the convention of evaluating the Allan deviation at a second.

The Deep Space Atomic Clock – an atomic clock launched in 2019 and a prototype for future interplanetary space missions – achieved $\sigma_y(\tau) \approx 2 \times 10^{-12}(\tau/1s)^{-1/2}$ for $\tau \lesssim 10^5$ s in a 2019 launch to a geostationary orbit[26]. The outer Solar System would avoid Earth magnetic field variations and the $9°$ temperature variations that it experienced, perhaps allowing the Deep Space Atomic Clock to achieve a noise level closer to its $10\times$ improved performance in the laboratory[26], a precision that has also been achieved by other space–certified clocks[27]. The best atomic clocks on Earth have achieved σ_y values of $\mathcal{O}(10^{-19})$ [28][29], and some studies have considered space–based gravitational wave detectors with atomic clocks of comparable precision[30][31].

The strain sensitivity given by equation (4) for timing precision of the best space qualified clocks is close to the sensitivity to detect the strain from equal mass $\gtrsim 10^8 M_\odot$ supermassive black hole mergers (as will be discussed in § 3). However, a couple orders of magnitude more precise atomic clocks are likely required to reach the strain sensitivities that could justify a spacecraft relying on atomic clocks. Due to the rapid development of terrestrial atomic clocks, a one–arm mission that relies on an atomic clock may become a possibility in the near future, and such a mission would be most motivated at $f \sim 1\mu$Hz owing to the larger strain amplitudes from anticipated astrophysical sources. We provide estimates for the mission sensitivity for different σ_y in § 3. We next review time–delay interferometry, an approach that essentially eliminates clock noise.

Two–arm and time–delay interferometry

The clock noise can be greatly reduced with a ≥ 2-arm interferometer using a technique called time–delay interferometry[32][33]. We consider a two-arm configuration with a home spacecraft broadcasting monochromatic waves (either with lasers or high–gain antennas) to two other

spacecraft, with these spacecraft a distance L_1 and L_2 away. This wave travels to the other spacecraft and then is sent back and compared to the reference wave at the home spacecraft. The phase differences measured from each of the two arms are

$$
\begin{aligned}
\phi_1 &= \phi_{\mathrm{os}}(t - 2L_1/c) - \phi_{\mathrm{os}}(t) + \frac{2\pi}{\lambda} L_1 h_1(t) + \phi_{1,\mathrm{N}}; \\
\phi_2 &= \phi_{\mathrm{os}}(t - 2L_2/c) - \phi_{\mathrm{os}}(t) + \frac{2\pi}{\lambda} L_2 h_2(t) + \phi_{2,\mathrm{N}},
\end{aligned}
\tag{5}
$$

following the same conventions as in equation (1). The data from a three-spacecraft configuration linked over two arms can be synthetically combined to create the following 'time-delay' observable:

$$
X(t) = [\phi_2(t - 2L_1/c) - \phi_2(t)] - [\phi_1(t - 2L_2/c) - \phi_1(t)].
\tag{6}
$$

Remarkably, the clock noise − ϕ_{os} − cancels in this expression − and, when considering a single frequency f and the limit $L_1 = L_2$, other noise sources are suppressed by the same factor as h_1 in this estimator − meaning that $X(t)$'s sensitivity to h_1 is the same as that of $\phi_1 - \phi_2$ but without clock noise.[2] For our calculations, the knowledge that $X(t)$ exists allows us to consider the interferometric observable $\phi_2 - \phi_1$ in the absence of clock noise.[3]

2.2. Radiometer noise

When limited by the strength of the incoming transmission, and deferring until § 4.1 some complications that arise for the heterodyne interferometry of lasers, a spacecraft can measure the incoming phase using a phase-lock loop with a half-bandwidth error power spectrum of e.g. [34]

$$
S_n(k) \equiv 2T^{-1} \langle |\tilde{\phi}_{1,N}|^2 \rangle = (C/N_0)^{-1},
\tag{7}
$$

where C/N_0 is the ratio of the carrier power to the unit-frequency noise power. Tildes denote the Fourier dual such that $\tilde{\phi}_N$ is the Fourier dual of the phase noise in equation (1). Equation (7) holds for both an interferometric setup using optical lasers or one with radio dishes, although what sets the noise is different in the two cases.

In the optical, C/N_0 is set by the shot noise of the received laser[35]:

$$
\begin{aligned}
[C/N_0]_{\mathrm{dB\text{-}Hz}}^{\mathrm{Optical}} &= 10 \log_{10} \frac{P_{rec}}{2\eta hc/\lambda}, \\
&= 33\mathrm{dB\text{-}Hz} + 10 \log_{10}\left(\frac{P_{em}}{10\mathrm{W}}\right) + 40 \log_{10}\left(\frac{D}{20\mathrm{cm}}\right) \\
&\quad - 10 \log_{10} \eta - 20 \log_{10}\left(\frac{L}{30\mathrm{AU}}\right) - 10 \log_{10}\left(\frac{\lambda}{1\mu\mathrm{m}}\right),
\end{aligned}
\tag{8}
$$

where P_{rec} is the received power of a Gaussian laser optimized to maximize the received power, η accounts for efficiency of the photodiodes and the fraction of the laser power at the heterodyne frequency, D is the mirror diameter, and we are using the engineering convention of characterizing C/N_0 in dB-Hz where $[C/N_0]_{\text{dB-Hz}} \equiv 10 \log_{10}(C/N_0)$. This paper considers $L = 10$ and 30 AU, and a LISA-like $\lambda = 1\mu$ m.

In the radio, the noise is characterized by the effective temperature of the system, T_{sys}, and given by

$$
\begin{aligned}
\underset{dB-Hz}{\text{Radio}} &= 10 \log_{10}\left(\frac{P_{rec}}{kT_{sys}} \right), \\
&= 34\text{dB-Hz} + 10 \log_{10}\left(\frac{P_{em}}{10W} \right) + 40 \log_{10}\left(\frac{D_{\text{eff}}}{5m} \right) \\
&\quad - 10 \log_{10}\left(\frac{T_{sys}}{50K} \right) - 20 \log_{10}\left(\frac{L}{30AU} \right) - 20 \log_{10}\left(\frac{\lambda}{1cm} \right),
\end{aligned}
\tag{9}
$$

where P_{em} is the emitted power and D_{eff} is the effective diameter of the radio dishes[34]. We have used the expressions in[36] to calculate P_{rec} from P_{em} for a radio dish. We will use Ka band transmissions with $\lambda = 1$cm for our estimates. For reference, the Voyager and Cassini probes had 4 meter diameter radio dishes, the SMAP spacecraft employed a fold-out 6 meter dish[37], the RadioAstron satellite that orbited to the Moon had a fold-out 10-meter dish[38]. Additionally, values of the receiver noise temperature of $\sim$ 50K are typical for narrow band receivers at room temperature, even space-qualified ones[39].4

To put the dB-Hz in equations (8) and (9) in context, which evaluate to $[C/N_0]_{dB-Hz} \sim 30 - 50$ for the parameter values discussed in this paper, LISA's pilot tones, whose phase is measured and used to correct timing jitter in the analog-to-digital conversion, have $[C/N_0]_{dB-Hz} = 75$ [40], a full four orders of magnitude larger C/N_0 than the signal for fiducial values in equations (8) and (9). The GRACE-FO mission's laser lock is able to operate at $[C/N_0]_{dB-Hz} = 61$ with minimal cycle slips[41]. Another point of reference is the X-band downlink of Cassini at 10AU to 34 m Deep Space Network antenna – used for the most precise Doppler tracking experiment – had $[C/N_0]_{dB-Hz} \approx 40 - 50$ [42]. Finally, the Voyager spacecraft at 140AU communicated with $[C/N_0]_{dB-Hz} = 30$ when communicating to a $D = 70$m Deep Space Network antenna[43].

Despite requiring lower C/N_0 than previous space missions, there has been substantial success at ranging with such weak electromagnetic signals. Indeed, dB-Hz ≈ 35 is known as the *acquisition threshold* for a receiver locking onto the Global Positioning System ranging code – roughly the threshold where a delay-lock loop can acquire the frequency and delay of a signal within 1ms by brute

force search over a grid of delays and frequencies motivated by typical terrestrial uncertainties[34]. As our concept's velocities and positions would be extremely well constrained, the threshold for acquisition of a ranging code would be even lower. (Of course, too small of a signal will result in cycle slipping in the phase-meter as discussed below.) Just like in these examples, the wave sent along each arm would likely be modulated by a pseudo-random code. Once a delay lock is established, the pseudo-random code decorrelates the signal from contaminating signals, such that we would anticipate phase measurements that are limited by either shot or thermal noise will be possible despite the small C/N_0.

Translating C/N_0 to a strain noises via equation (7) yields

$$\tilde{\phi}_{\mathrm{rms}} = \sqrt{S_n(k)} = 0.01 \times 10^{-([\mathrm{C/N_0}]_{\mathrm{dB-Hz}}-40)/20} \ \mathrm{rad \ Hz}^{-1/2}, \tag{10}$$

which must satisfy the requirement that $(T_\phi/2)^{-1/2}\tilde{\phi}_{\mathrm{rms}} \lesssim 0.1$ for there to be a phase lock with negligible cycle slipping for typical parameters considered in this paper, where T_ϕ is the effective averaging-time for the phase measurement made by the phase lock loop $2/T_\phi$ is the bandwidth of the phase-lock loop[44][34]. This condition and equation (10) means that our concepts require $T_\phi \gtrsim 10^{-2}$ s, with the exact value depending on their C/N_0. However, T_ϕ cannot be longer than the time over which the phase changes by an order one value because of displacements from accelerations, clock drifts, or frequency drifts in the laser. The mean acceleration from the Sun we find leads to displacements of a waveperiod over $\sim 10(r/30\mathrm{AU})$ s for the laser case and over a much longer period for the radio one. The maximum T_ϕ may also set by clock noise, although we find that this is unlikely to prevent values of $T_\phi \sim 10^{-2}$ s and even possibly much larger, or the lasers' frequency stability for the laser case. Defining S_f to be the laser frequency noise power, we find that $S_f T_\phi \lesssim 0.3$ must be satisfied at $f \gtrsim T_\phi^{-1}$ to not significantly impact the signal-to-noise of a phase measurement as, in a simplified model for the phase lock where the phase is measured over a tophat window of width T_ϕ, we find the requirement for minimal cycle slips changes to $(T_\phi/2)^{-1/2}\tilde{\phi}_{\mathrm{rms}} \exp[S_f T_\phi] \lesssim 0.1$ when measuring the phase from two interfering lasers, both with the same white frequency noise S_f. For $T_\phi = 10^{-2}$ s, this condition requires a factor of $\gtrsim 5$ improvement over the requirement on $\sqrt{S_F}$ of LISA's lasers, which have the requirement $\sqrt{S_f} < 30\mathrm{Hz/Hz}^{1/2}$ over pertinent frequencies. Improved frequency noise could potentially be achieved with greater thermal control of the resonant cavity or choosing materials with smaller thermal expansion coefficients[45].5 The GRACE-FO mission lasers achieved frequency stability of $\sqrt{S_f} \sim 0.4(f/1\mathrm{Hz})^{-1}\mathrm{Hz/Hz}^{1/2}$ [41].

Translating equation (10) one step further into a displacement noise yields

$$\tilde{\Delta}x_{\mathrm{rms}} = \frac{\lambda\tilde{\phi}_{\mathrm{rms}}}{2\pi} = \overbrace{(1.6\times10^{-3}}^{\lambda=1\mathrm{cm}}, \overbrace{1.6\times10^{-7}}^{\lambda=1\mu\mathrm{m}}) \ \mathrm{cm} \ \mathrm{Hz}^{-1/2} \times 10^{-([\mathrm{C/N_0}]_{\mathrm{dB-Hz}}-40)/20}, \qquad (11)$$

where the two displacement noise values correspond to $\lambda = 1$ cm − the Ka band radio regularly used for ranging − $\lambda = 1\mu$ m − a LISA-like near infrared laser. For reference, LISA aims to achieve $\tilde{\phi}_{\mathrm{rms}} = 9\times10^{-6}$ rad Hz$^{-1/2}$ and $\tilde{\Delta}x_{\mathrm{rms}} = 15\times10^{-10}$ cm Hz$^{-1/2}$ [7].

Finally, these estimates translate into a precision for how well the gravitational wave strain can be measured. The long wavelength strain noise for a single arm is

$$\tilde{h}_{\mathrm{rms}}^{\mathrm{LW}} = \frac{\sqrt{2}\tilde{\Delta}x_{\mathrm{rms}}}{L},$$
$$= \overbrace{(5\times10^{-18}}^{\lambda=1\mathrm{cm}}, \overbrace{5\times10^{-22}}^{\lambda=1\mu\mathrm{m}}) \ \mathrm{Hz}^{-1/2} \ \mathcal{A}\left(\frac{L}{30\mathrm{AU}}\right)^{-1} \times 10^{-([C/N_0]_{dB-Hz}-40)/20}. \qquad (12)$$

We will eventually use a transfer function that converts the single-arm noise in the low f limit to a two-arm time-delay interferometry measurement that is applicable at all f (§ 3). The factor of $\sqrt{2}$ in the first expression is because there are uncorrelated measurements of the phase at both spacecraft in an arm. Here, $\mathcal{A}$ encapsulates the increase in the phase error from using phase measurements at two wavelengths to eliminate plasma dispersion. Since plasma dispersion is negligible for lasers, for the laser setup a single wavelength would be used and $\mathcal{A} = 1$. We show in Appendix A that $\mathcal{A} \approx 1.5(1.8)$ if wavelengths differing by a factor of 4 (2) are used when referenced to the shorter wavelength, assuming T_{sys} and D_{eff} are the same at both wavelengths.

Another possibility is to use nanosecond laser pulses as a clock, rather than the carrier phase timing considered so far. Laser pulses would be more noisy for the Solar System-scale baselines we consider since the signal can no longer be matched to a template phase, with

$$\tilde{h}_{\mathrm{rms}}^{\mathrm{LW}}\Big|_{\mathrm{laser-pulses}} \sim 2\times10^{-14}\mathrm{Hz}^{-1/2}\left(\frac{\lambda}{1\mu\mathrm{m}}\right)^{3/2}\left(\frac{L}{30\mathrm{AU}}\right)^{2}\left(\frac{D_1 D_2}{[1\mathrm{m}]^2}\right)^{-3}\left(\frac{P_{\mathrm{em}}}{10\mathrm{W}}\right)^{-3/2}, \qquad (13)$$

where D_1 and D_2 are the sizes of the mirrors on the emitting and receiving telescopes, and this assumes the laser pulses have a width equal to the time between pulses cf. their eqn. 95[20]. We return to this possibility in § 3.3.

2.3. Acceleration noise

In this section, we consider different sources of acceleration on the spacecraft. We quantify this in terms of the acceleration power spectrum on one detector, defined as $S_a(f) \equiv 2T^{-1}\langle|\tilde{a}(f)|^2\rangle$, where $\tilde{a}(f)$ is the Fourier transform of the acceleration over time T. Figure 2 summarizes our estimates for the important acceleration sources, assuming a fiducial spacecraft effective area over mass of $A_{\mathrm{eff}}/M = 0.01$ m^2 kg^{-1} – justified further in § 3.1 – and spacecraft at a heliocentric radius of $r = 30$ AU. These include solar irradiance variations, drag from the solar wind, Lorentz forces on the spacecraft assuming the maximum possible spacecraft charge, and dust for two maximum dust masses (as explained later, the lower of the two dust curves is the more applicable). Figure 2 also shows the acceleration control specification of the Gravitational Reference Sensor (GRS) on LISA[7]. A LISA requirement is to achieve the acceleration control shown by this curve to frequencies as low as 10^{-4} Hz, with the goal to achieve this to 2×10^{-5} Hz. This figure shows that at 30AU the different sources of acceleration are only an order of magnitude larger than the sensitivity of the GRS at 10^{-4} Hz. Furthermore, since the dominant accelerations are radial with respect to the Sun, additional geometric cancellation is likely when optimizing the spacecraft orientations. This motivates our overall direction of considering an outer Solar System instrument without a precise accelerometer.

In what follows, we discuss each source of acceleration, ordered roughly by importance.
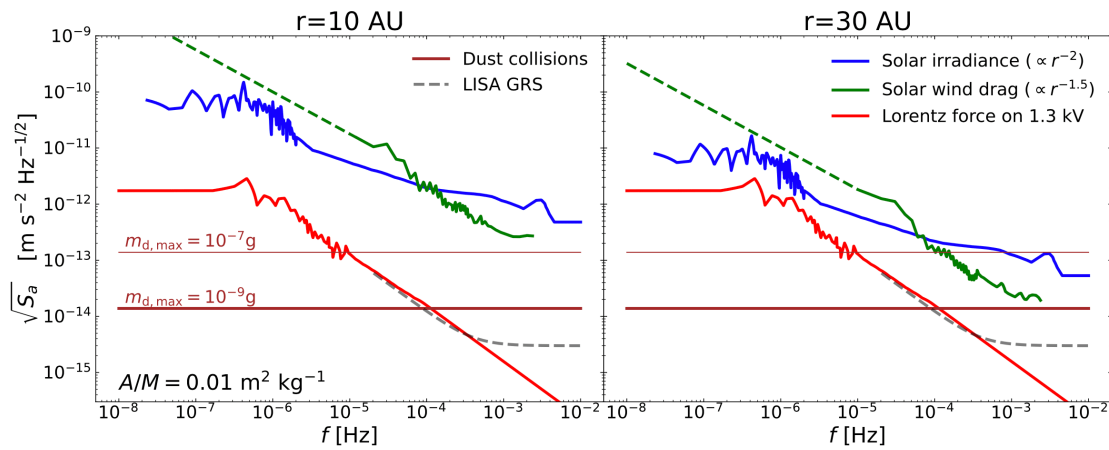
Figure 2. Square root of the power spectrum (the amplitude spectral density) of the most important acceleration sources. The calculations assume a spacecraft at a solar distance of $r = 10$ AU (left panel) and $r = 30$ AU (right panel) with a mass of $M = 10^3$ kg and an effective area of $A_{\text{eff}} = 10 \, \text{m}^2$. As irradiance and solar wind are directed radially, a reduction in these forces can be achieved by orienting the arms to be more perpendicular to these radial flows. Two different maximum dust masses are shown, reflecting uncertainties in the measured distribution. The contamination of accelerations from $m_{d,\max} > 10^{-9}$ g grains likely can be cleaned. Also shown are the acceleration goal of the LISA Gravitational Reference Sensor (GRS).

2.3.1. Solar irradiance

During active periods, the Sun shows 0.2% peak-to-peak irradiance variations on the timescale of its 27-day rotation period plus fluctuations over a broad range of timescales. Figure 2 shows the power spectrum of irradiance variations measured using the Variability of Solar Irradiance and Gravity Oscillations instrument on the Solar and Heliospheric Observatory VIRGO/SOHO; [46], converting the radiation force to spacecraft acceleration.[6] We use measurements over $1996 - 1997$ that were near the minimum of solar activity [46]. The amplitude of the square root of the irradiance power spectrum varies by a factor of three at $0.1 - 10\mu$ Hz over the eleven-year solar cycle, with smaller variations at $> 10\mu$ Hz.

2.3.2. Solar wind drag

We find that drag from the solar wind is the other important source of accelerations in addition to irradiance variations. While the mean drag force scales as r^{-2} with distance from the Sun, the

inhomogeneous component falls off somewhat less quickly at $r \gtrsim 10$ AU owing to the amplitude of the fractional density fluctuations growing with r. From Fourier transforming the time series along its trajectory, Voyager 2 finds a 1D power spectrum of electron density fluctuations with the approximate form

$$P_e^{1D}(f,r) \approx P_{e,0}^{1D} \left(\frac{f}{10^{-5}\,\mathrm{Hz}} \right)^{-\beta} \left(\frac{r}{30\mathrm{AU}} \right)^{-3}, \tag{14}$$

where $P_{e,0}^{1D} \approx 10^{11.1}\,\mathrm{m}^{-6}\,\mathrm{Hz}^{-1}$, and we find using the measurements of [47] that the -3 index approximates the radial scaling over $10 - 50$ AU.

We can convert from an electron density power to a (radial) spacecraft acceleration power using

$$\sqrt{S_a} = \mu m_p v_{sw}^2 A_{\mathrm{eff}} M^{-1} \sqrt{P_e^{1D}(f,r)}. \tag{15}$$

If we take our approximate form for the power given by equation (14), a mean molecular weight of $\mu = 1.2$, and $v_{sw} = 500$ km s^{-1} for the velocity of the solar wind, we can rewrite equation (15) as

$$\begin{aligned}
\sqrt{S_a} =& 1.2 \times 10^{-12}\,\mathrm{m\,s}^{-2}\,\mathrm{Hz}^{-1/2} \left(\frac{\mathrm{A_{eff}/M}}{10^{-2}\,\mathrm{m^2\,kg^{-1}}} \right)^{1/2} \left(\frac{\mathrm{P_{e,0}^{1D}}}{10^{11.1}\,\mathrm{m^{-6}Hz^{-1}}} \right)^{1/2} \\
& \times \left(\frac{f}{10^{-5}\,\mathrm{Hz}} \right)^{-\beta/2} \left(\frac{r}{30\mathrm{AU}} \right)^{-1.5}.
\end{aligned} \tag{16}$$

However, rather than assuming some power-law spectrum as in equation (16), we can compute the drag using the actual electron power that Voyager 2 measured using the measurements presented in[47]. Figure 2 shows just this at 30 AU assuming a spacecraft effective area to mass of $A_{\mathrm{eff}}/M = 0.01$ m^2 kg^{-1}, also using equation (15). Figure 2 illustrates that Voyager 2's electron power spectrum is not exactly a power law. Between $10^{-4} - 10^{-2}$ Hz,[47] finds $\beta \approx 2$. At higher frequencies, the spectrum is more consistent with a Kolmogorov turbulence-like $\beta = 5/3$ spectrum. There is the additional complication that[47] did not consider $f < 10^{-5}$ Hz. While we think it would be possible to use the Voyager data to probe these lower frequencies, for this study we extrapolate thier measurement with the index $\beta = 1.5$. Extrapolating with a flatter scaling than that observed at higher frequencies is motivated by the power spectrum of the solar wind within several astronomical units, which tends to have a power spectrum of $\beta \approx 1$ at these low frequencies. (The properties of the solar wind are likely to be largely maintained as it advects into the outer Solar System.) Additionally, in the solar wind, the power spectrum of density fluctuations is often similar to that of magnetic field

fluctuations, and the power spectrum of the magnetic field amplitude is observed to flatten at sub-μ Hz frequencies[48].7

2.3.3. Dust

Each collision with a dust grain results in a change of velocity of the spacecraft of $\Delta v_i = m_{d,i} v_d / M$, where $m_{d,i}$ is the mass of the ith dust grain and M the mass of the spacecraft. We treat all grains as having the same velocity of $v_d = 20$ km s^{-1}, motivated by the interstellar flow of dust that is found to dominate the dust population in the outer Solar System[49]. If the interferometer arm is not oriented in the flow direction of the interplanetary dust (which has been found to be moving in roughly the ecliptic with longitude $250°$), there is a geometric suppression relative to our estimates.

The density distribution of interplanetary dust is found to be roughly constant per $\log$ mass between $m_d = 10^{-12}$ and 10^{-9} g with $d\rho_d/d\ln m_d = 1.2 \times 10^{-27}$ g cm^{-3}[50]. The grain size distribution has not been measured above 10^{-9} g. We assume $d\rho_d/d\ln m_d = 1.2 \times 10^{-27}$ g cm^{-3} up to $m_{d,\max}$. Since each dust collision can be approximated as causing a step function in the spacecraft velocity, the acceleration of the spacecraft dV/dt is then a sum of Dirac δ-functions at the collision time t_i, which in Fourier space is $d\tilde{V}/dt = \sum_i \Delta v_{d,i} \exp[-i\omega(t - t_i)]$. If we treat each grain as uncorrelated in time, then the acceleration power spectrum is

$$\sqrt{S_a} \equiv \left(2T^{-1}\langle|\frac{d\tilde{V}}{dt}|^2\rangle\right)^{1/2} = \left(2\int_0^{m_{d,\max}} d\ln m_d \times d\rho_d/d\ln m_d \times [\Delta v(m_d)]^2\right)^{1/2}, \qquad (17)$$

$$= 9.8 \times 10^{-15} \text{ m s}^{-2} \text{ Hz}^{-1/2} \left(\frac{m_{d,\max}}{10^{-9}\text{g}} \frac{d\rho_d/d\ln m_d}{1.2 \times 10^{-27}\text{cm}^{-3}}\right)^{1/2} \left(\frac{M}{10^3\text{kg}}\right)^{-1} \left(\frac{A}{10\text{m}^2}\right)^{1/2}. \qquad (18)$$

Figure 2 shows that the dust acceleration power given by equation (18) is a subdominant source of acceleration for our fiducial spacecraft specifications. Only if we increase the maximum mass to 10^{-7}g does it become comparable to other sources of acceleration at $r = 30$AU.

The accelerations from more massive dust particles can be fit and their contribution to the noise power removed. The 'characteristic strain' of a single dust event provides an estimate for what dust masses should be detectable and is given by $h_c^{\text{dust}} = \Delta v/(2\pi^2 f^2 T_{\text{fit}} x)$, where T_{fit} is the period over which other dust collisions contribute less to the acceleration relative to the grain in question. To the extent that the characteristic strain falls above the strain noise, which we find is the case for $m_d \sim 10^{-8}(10^{-9})$g if $T_{\text{fit}} = 10^4(10^6)$s, the acceleration from the collisions with the dust grain can be fit for and removed. With our above assumptions about $d\rho_d/d\ln m_d$, grains of mass m_d strike the

spacecraft every $\sim 4 \times 10^6 \mathrm{s}(m_d/10^{-9}\mathrm{g})^{-1}(A_{\mathrm{eff}}/10\mathrm{m}^2)$, suggesting that dust collisions with $\gtrsim 10^{-9}\mathrm{g}$ grains can be cleaned. We find this statement is relatively independent of the radiometer noise for typical values considered in this paper, as h_c^{dust} has a similar scaling with f to the total acceleration noise. This indicates that this source of anomalous accelerations would be removable for dust grain masses that could lead to significant acceleration noise relative to other acceleration sources.

2.3.4. Spacecraft charging

A spacecraft will build up charge as it flows through the interplanetary plasma. The Lorentz force of the interplanetary magnetic field will then impart accelerations on the spacecraft. The maximum possible charge Z_{max} is roughly the charge able to repel solar wind protons from striking the spacecraft $1/2 m_p v_{sw}^2 = Z_{\mathrm{max}}e^2/R_{sc}$, where e is the electron charge, m_p the proton mass, v_{sw} the velocity of the solar wind, and R_{sc} the characteristic size of the spacecraft. We find for a velocity characteristic of the solar wind of $v_{sw} = 500\mathrm{km}\ \mathrm{s}^{-1}$, this results in a maximum voltage of $V \sim Z_{\mathrm{max}}e/R_{sc} = 1300\mathrm{V}$.

The magnitude of both the homogeneous and inhomogeneous magnetic fields in the outer Solar System are on the order of a μGauss, falling off by only a factor of two from 1AU to 20AU[48]. The magnetic field power spectrum is also found to maintain a similar spectrum with distance from the Sun. This near constancy supports our approach of using the magnetic field power spectrum measured by the Voyager 1 spacecraft at $6.1 - 8.9\mathrm{AU}$ to compute the Lorentz force on the spacecraft at all the solar radii considered. This acceleration power for the maximum spacecraft charge is shown in Figure 2, assuming an effective spacecraft extent of $R_{sc} = 2\mathrm{m}$ to calculate Z_{max} and then the acceleration power along an arm is given by $\sqrt{S_a} = Z_{\mathrm{max}}v_{sw}\sqrt{P_B(f,r)}/(\sqrt{3}M)$, assuming isotropic B –field perturbations. However, this is likely an overestimate as interplanetary spacecraft are designed to have voltages that are likely to be closer to a tenth of our estimate for the maximum[51].

2.3.5. Gravity from asteroids and larger bodies

The gravitational attraction of asteroids will be another source accelerations. Using the JPL Small–Body Database,[52] computed the acceleration power from asteroids for spacecraft at 30 AU from the Sun, finding an acceleration power that is absolutely negligible ($\sim 10^{-18}\ \mathrm{m\ s^{-2}\ Hz^{-1/2}}$ at $10^{-7}\mathrm{Hz}$ and even smaller values at higher frequencies). However, this catalog of asteroids is wildly incomplete at 30 AU. They also considered a spacecraft at 1 AU where catalogs are more complete, and found

$10^{-12}\,\mathrm{m\,s^{-2}\,Hz^{-1/2}}$ at $< 2 \times 10^{-7}\,\mathrm{Hz}$, dropping to $10^{-14}\,\mathrm{m\,s^{-2}\,Hz^{-1/2}}$ at $4 \times 10^{-7}\,\mathrm{Hz}$. Given that even these 1 AU values are subdominant when compared to the other outer Solar System acceleration sources we compute, asteroids are unlikely to be an important acceleration source.

Displacements owing to gravitational pulls from the Sun and planets should be correctable, as the spacecraft ranging system would measure spacecraft separations to centimeter precision[36]. Long-term trends from these pulls on the $\gtrsim$ year orbital time scales of these bodies can be fit for and removed from contaminating the $f \gg \mathrm{yr}^{-1}$ frequencies of interest.

2.3.6. Off-gassing and other spacecraft emissions

Because our spacecraft would be in such a low acceleration environment, a concern is that off-gassing either from thrusters or from other components in the spacecraft could drive a substantial acceleration. Since external accelerations are $\sqrt{fS_a} \sim 10^{-14}\,\mathrm{m\,s^{-2}}$ for the wave periods of interest, 10 picoNewton of thrust over these periods could result in increased noise.

Thrusters are necessary to dissipate angular momentum on the reaction wheels on week to month times, but for the science operation would be generally turned off. They can be turned on to dissipate angular momentum during a science run, and then their delta-function like acceleration profile can be fit and removed just like for dust grain collisions. When turned off, micro-Newton thrusters can only leak at a part in 10^5 of their baseline thrust to achieve the 10 picoNewton specification. Additionally, consider the off-gassing of ~ 280 K gas from within the thermally regulated spacecraft. If the spacecraft emits in a single direction, the acceleration would be $a_{\mathrm{off-gas}} \sim \Delta m f v / M$ for Δm emitted over time f^{-1}, or $a_{\mathrm{off-gas}} \sim 10^{-14}(\Delta m / 10^{-4}\mathrm{g})(f/10^{-6}\mathrm{Hz})(M/10^3\mathrm{kg})^{-1}\mathrm{m\,s^{-2}}$, evaluated at values that yield a similar acceleration to what we find for external accelerations at a microHertz ($\sqrt{fS_a} \sim 10^{-14}\,\mathrm{m\,s^{-2}}$). As the acceleration power from external sources decreases to higher frequencies, shorter period off-gassing events may be even more problematic. Ventilation and thermal control systems that are designed to off-gas perpendicular to the arms and maintain a stable environment over the gravitational wave periods of interest would likely be required for such precision.

3. Strain power sensitivity

The carrier-to-noise ratio discussed in § 2.2 and the acceleration noise in § 2.3 allow us to estimate the gravitational wave strain sensitivity. Namely, the radiometer noise power, S_n, and acceleration

power, S_a, can be related to the interferometer's sensitivity to the polarization- and sky-averaged gravitational wave strain power at a specific frequency (e.g. [53][54]). The gravitational wave instrument's noise when performing the average that generates this strain power is

$$S_h(f) = \frac{2}{L^2 R(f)} \left(\frac{2\mathcal{A}^2 S_n}{(2\pi f)^2} + \frac{4\left[1 + \cos^2(2\pi f L/c)\right] S_a}{(2\pi f)^4} \right), \tag{19}$$

where the factor of $2\mathcal{A}^2$ is because there are two spacecraft in an arm with independent radiometer noise and $\mathcal{A}$ encapsulates the increase in error from fitting out plasma dispersion (and is only different from unity in the radio). The factor $4\left[1 + \cos^2(2\pi f L/c)\right]$ is because the acceleration of a spacecraft contributes to a displacement that coherently impacts the phase both in the incoming and outgoing directions. The function $R(f)$ is a transfer function that transforms the single-arm noise in the long-wavelength limit (and in which the gravitational wave is propagating orthogonally) to the noise power seen when averaging the instrument's strain response over all angles. We will first consider the instrument to be a two-arm (time-delay) interferometer and later consider one-arm configurations. The overall factor of two out front of equation (19) follows the conventions for time-delay interferometry where the phase observable is a difference between the two independent arms, although we will define $R(f)$ for one-arm configurations to cancel this factor of two so that this equation still applies. We use the analytic form for $R(f)$ calculated in [53], and for our time-delay interferometer configurations assume an angle between the arms of $90°$.[8] Equation (19) assumes the noise and accelerations are independent between spacecraft: This will not be true for the acceleration noise on the intermediate spacecraft that joins both arms in the time-delayed inteferometry configuration, as the radial accelerations from solar irradiance and the solar wind will project onto both interferometer arms.

In what follows, we present the sensitivity for both a two-arm time-delay interferometry setup (§ 3.1) as well as a setup with a single-arm and atomic clock (§ 3.2), and finally consider the 'Doppler tracking' architecture in which the single-arm is anchored to Earth (§ 3.3).

3.1. Two-arm time-delay interferometry forecasts

The left and right panels in Figure 3 show respectively the gravitational wave strain sensitivities calculated from equation (19) for the proposed concept at a solar distance of $r = 10$ AU and $r = 30$ AU, assuming the same arm lengths as the solar distance, e.g. $L = r$. The calculations assume a geometric suppression of the radial accelerations from the Sun's radiation and drag forces by 0.5, as would occur

if each interferometer arm was a side of a distinct equilateral triangle with the other two sides the Sun–spacecraft distances. If instead the configuration were an isosceles triangle with two satellites at distance r from the Sun, the suppression factor would be $L/2r$. These calculations additionally assume an effective area-to-mass ratio for the spacecraft of $A_{\mathrm{eff}}/M = 0.01 \text{ m}^2 \text{ kg}^{-1}$, which for example could be achieved with a spacecraft with $A_{\mathrm{eff}} = 10 \text{ m}^2$ and mass of $M = 1000$ kg (perhaps more applicable for the radio dish case) or $A_{\mathrm{eff}} = 3 \text{ m}^2$ and $M = 300$ kg (perhaps applicable to the laser case and similar to each LISA spacecraft once the solar panels are removed).
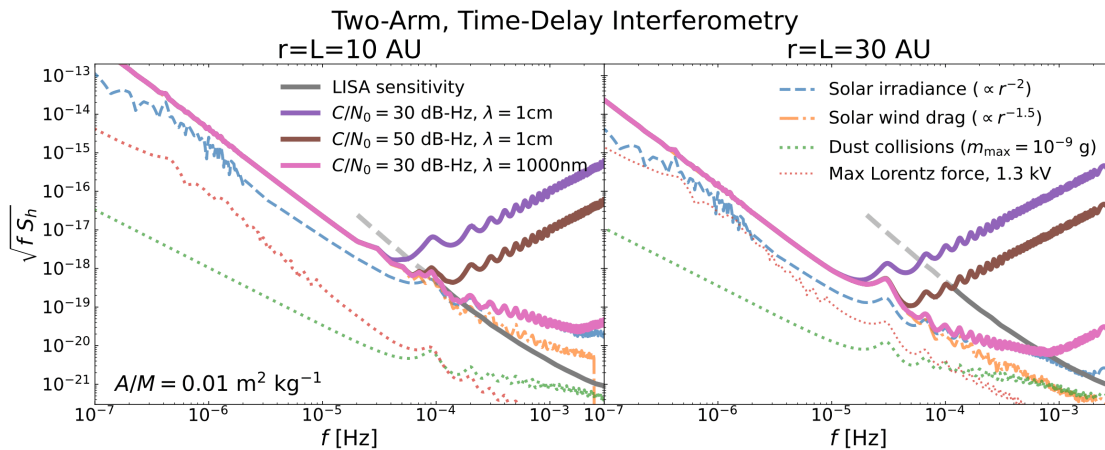
Figure 3. Gravitational wave strain sensitivities for the **first design architecture: the two-arm time-delay interferometry concept**, with $r = L = 10$ AU (left panel) and $r = L = 30$ AU (right panel). The calculations assume an effective area to mass ratio for the spacecraft of $A_{\mathrm{eff}}/M = 0.01 \text{ m}^2 \text{ kg}^{-1}$ and a geometric suppression of 0.5, as would occur if each interferometer arm was a side of an equilateral triangle with the other two sides the Sun–spacecraft distances. The curves show the contributions from accelerations owing to solar irradiance variations, solar wind drag, the maximum possible Lorentz force from spacecraft charging, and dust collisions assuming $m_{d,\mathrm{max}} = 10^{-9}$ g and $A_{\mathrm{eff}} = 10 \text{ m}^2$. Also shown by the thick curves is the total strain error for radio and laser transmissions with different carrier-to-noise ratios (C/N_0), where we have excluded the smaller contributions to the accelerations from dust collisions and spacecraft charging. A requirement of the LISA mission is to achieve the sensitivity shown by the gray solid curve for $f > 10^{-4}$ Hz, with the goal to be sensitive to $f > 2 \times 10^{-5}$ Hz as illustrated by the dashed extension. The total strain sensitivity lines are repeated in Fig. 4.

The curves in Figure 3 show the contributions to the noise from accelerations owing to solar irradiance variations, the solar wind, the maximum possible Lorentz force from spacecraft charging, and dust

collisions assuming $m_{d,\max} = 10^{-9}$g and $A_{\mathrm{eff}} = 10\mathrm{m}^2$. Also shown by the thick curves is the total strain error for radio and laser transmissions with different carrier-to-noise ratios (C/N_0). Those that are for $\lambda = 1$cm assume carrier-to-noise ratios (C/N_0) of 30dB-Hz and 50dB-Hz (§ 2.2) and $\mathcal{A} = 1.5$ (Appendix A). Also shown is a laser effort with $\lambda = 1\mu$m and 30dB-Hz. The noise is smaller for the case of laser links compared to radio ones at $f \gtrsim 5 \times 10^{-5}$Hz, whereas at lower frequencies the sensitives are similar as acceleration noise dominates. A major goal of the proposed concepts would be to fill in the portion of the gravitational wave spectrum not probed by LISA. The LISA mission (which has three arms and, hence, more interferometric observables than our one-arm concepts) is required to achieve the sensitivity shown by the gray solid curve for $f > 10^{-4}$ Hz, with the goal for LISA to be sensitive to $f > 2 \times 10^{-5}$ Hz as illustrated by the dashed extension.

Figure 4 shows how these sensitivity projections compare to the gravitational wave signals from astrophysical sources, where we have taken 50dB-Hz for the $r = L = 10$AU case (left panel) and 30 dB-Hz for the $r = L = 30$AU one (right panel). The green curves show the characteristic strain of equal-mass supermassive black hole mergers at $z = 3$ with the initial mass of each black hole annotated and showing the five years before merger[55]. The characteristic strain is defined such that the integral over $\log f$ of the ratio of the characteristic strain to the concept's noise power equals the square of the signal-to-noise ratio for detection.

Figure 4 also shows the estimate for the Galactic white dwarf binary stochastic gravitational wave background (WDB GWB) from[56], which we find to be a factor of two lower than the estimate of[57]. The stochastic background is defined as the background where the density of sources is too high in each spectral bin over a ~ 5yr observing period for cleaning to be effective and hence this represents essentially an irreducible noise[56]. Frequencies of $\sim 10^{-4}$Hz correspond to orbital periods for which gravitational waves in stellar mass systems are not able to drive coalescence in ~ 1Gyr. Since this is approaching the maximum age of stellar systems, at lower frequencies (where the coalescence time is even longer) the gravitational wave background from stellar binaries will be shaped by the initial distribution of orbital properties and not just the limit where this distribution is set by gravitational radiation as these curves assume.

Below 10^{-4} the unresolvable massive black hole binary stochastic gravitational wave background (MBHB GWB) at the centers of galaxies likely exceeds the background from stellar binaries. The 'most likely' estimate for the MBHB GWB from[58] is shown by the darker grey solid – and we find the total background in this estimate is in agreement with pulsar timing array observations at $f = 3 \times 10^{-8}$Hz

e.g. [4]. [58] also provided 'maximum' and 'minimum' bounds on the MBHB GWB, with each bound shifting the amplitude of $\sqrt{S_h}$ by a factor of ~ 5 relative to the 'most likely' model.

We can also forecast the number of astrophysical sources to which this concept would be sensitive, using the fact that the strain sensitivities we are forecasting at $f \lesssim 0.5 \times 10^{-4}$ Hz are somewhat similar to the μ-Ares concept[9], particularly for our $r = L = 30$ AU configuration. Over a ten year period, μ-Ares forecasts detecting $\mathcal{O}(1000)$ inspiralling supermassive black holes, finding $\mathcal{O}(100)$ black hole binaries in the Milky Way, and observing all stars and compact objects that would merge with Sag A* in $10^6 - 10^8$ year. Our most sensitive designs would be capable of similar returns.

Figure 4 also shows curves for a more aggressive suppression factor of 0.05. Such a suppression would likely require monitoring and then correcting the radiation from the Sun and the solar plasma with additional onboard instrumentation. In fact, the Lagrange concept, proposed as a potentially cheaper replacement to LISA by abandoning drag-free control, found that such instrumentation could potentially produce a factor of 100 suppression beyond the factor of ~ 10 they aimed to achieve geometrically[21].
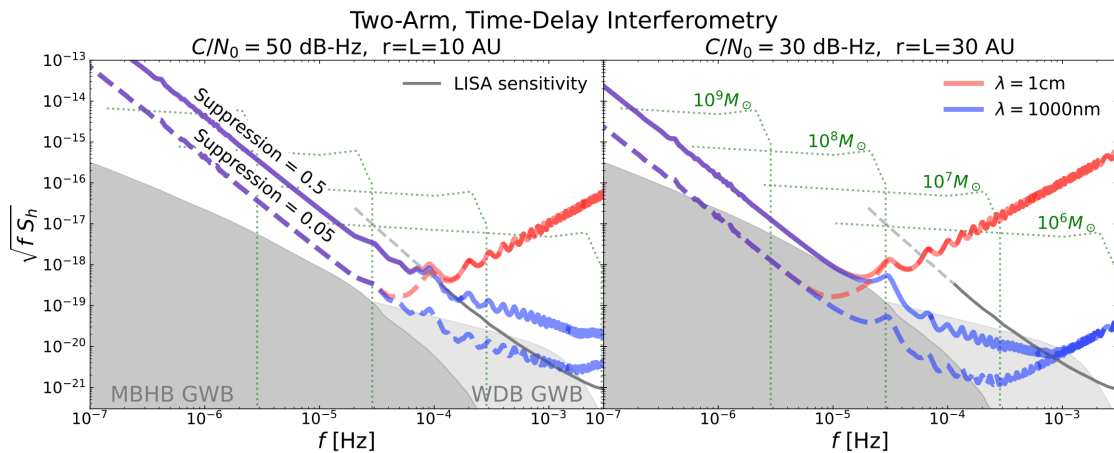
Figure 4. Gravitational wave sensitivity for the same time-delay interferometry architectures as shown in Fig. 3 with $r = L = 10$ AU (left panel) and $r = L = 30$ AU (right panel) and a geometric suppression of 0.5, plus the same cases but assuming a more aggressive 0.05 suppression factor. Also shown are different astrophysical sources: estimates for the galactic white dwarf binary stochastic gravitational wave background (WDB GWB; [56]), the massive black hole binary stochastic gravitational wave background (MBHB GWB; [58]), and the characteristic strain within 5 yr of coalescence from equal-mass black hole mergers at $z = 3$, where the pre-merger black hole masses are annotated.

doi.org/10.32388/L6RW3G.2

3.2. Single-arm with atomic clock forecasts

A simpler mission would use a single arm, but a single-arm design would also require the inclusion of an atomic clock to reach interesting sensitivities. Figure 5 considers this one-arm setup for $r = L = 10$ and 30 AU, but Note that the phase noise power induced by clock noise is independent of the baseline length for $fL \ll 1$. For this calculation, we generalize equation (19) to also include the clock noise given by equation (3), requiring the replacement $2\mathcal{A}^2 S_n \to 2\mathcal{A}^2 S_n + S_{os,tot}$, where $S_{os,tot}$ is given by equation (3). This assumes the signal travels along one arm and, then, is transponded back to the home satellite that has a precise clock. The sensitivity curves are for the $\lambda = 1$ cm radio case for the specified C/N_0, but we note the laser and radio sensitivities are the same to the extent that the sensitivity is limited by clock noise rather than radiometer noise.
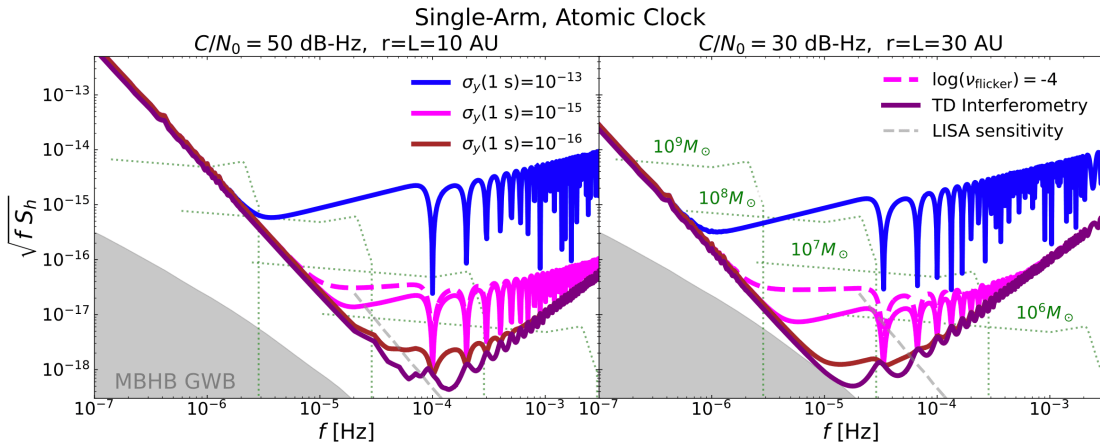
Figure 5. Similar to Figure 4 except showing the gravitational wave strain sensitivities for the **second design architecture: the single-arm atomic clock concept**. Additionally, the same $\lambda = 1$ cm time-delay interferometry curve as in Figure 4 is included for comparison. The curves consider the $\lambda = 1$ cm radio case, although the sensitivity would not be different for the laser case to the extent that clock noise limits the sensitivity. Allan deviations for $\tau = 1$ s of $\sigma_y = 10^{-13}$ are similar to the Deep Space Atomic Clock, whereas the most precise atomic clocks on Earth achieve $\sigma_y \sim 10^{-19}$. The dashed pink curve shows what happens to the $\sigma_y(\tau = 1s) = 10^{-15}$ case if the clock enters the flicker frequency noise regime at $f < 10^{-4}$ Hz (rather than white frequency noise as otherwise assumed). Phase measurements referenced to a local clock in each arm would achieve nearly the sensitivity of time-delay interferometry with two arms if the clock has $\sigma_y \lesssim 10^{-16}$. All sensitivity curves assume a geometric suppression of the accelerations by a factor of 0.5.

The clock noise is comparable to radiometer noise in the curves that assume the most precise clock with $\sigma_y(\tau = 1\text{s}) = 10^{-16}$, as can be seen by noting their sensitivity is comparable to the corresponding time-delay interferometry curve. (The transfer function $R(f)$ is modestly different compared to the two-arm concept.[9] At larger f, distinct downward spikes in the noise are present at $2Lf = n$ for integer n, due to the clock noise canceling in the noise power. One can see that the amplitude of these downward spikes decreases with decreasing σ_y as clock noise becomes less of a limiting factor.

For the case of radio transmissions, phase measurements referenced to a local clock in each arm would achieve nearly the sensitivity that would be achieved by time-delay interferometry if the clock has $\sigma_y \lesssim 10^{-16}$. Allan deviations for $\tau = 1\text{s}$ of $\sigma_y = 10^{-13}$ are similar to the Deep Space Atomic Clock, whereas $\sigma_y = 10^{-16}$ has been bested by three orders of magnitude by the most precise Earth-based clocks[28]. The calculations discussed so far assume $\sigma_y^2 \propto \tau^{-1}$ as applies in the case of white frequency modulation noise, a scaling demonstrated to hold for $\tau < 10^5\text{s}$ in the case of the Deep Space Atomic Clock (but sometimes only to $\tau \sim 10^4\text{s}$ for the most precise atomic clocks). When white frequency modulation noise no longer applies, clocks often enter the 'flicker frequency modulation' noise regime where $\sigma_y(\tau)$ is constant with τ resulting in the clock noise power flattening in f by one index. The pink dashed curves in Figure 5 show that transitioning to this flicker clock noise scaling at $f < 10^{-4}\text{Hz}$ for the case $\sigma_y(\tau = 1\text{s}) = 10^{-15}$ has a relatively modest affect on the sensitivity.

## 3.3. Doppler tracking forecasts

A potentially simpler design uses Earth for one element in the single-arm setup. This approach has an extensive history and is called Doppler tracking (for a review, see[59]). Beyond requiring just a single spacecraft, such a setup has several other advantages: 1) the Earth station's non-gravitational accelerations are potentially negligible, 2) more substantial resources are available at the Earth station, allowing kilowatt up-links, larger collecting areas, and cryogenic cooling, 3) the Earth station can be equipped with an ultra-precise atomic clock. However, the mechanical distortions of the instruments from gravity and terrestrial temperature cycles are larger on Earth, and an Earth station has to further contend with propagation delays due to the Earth's atmosphere. For reference, our estimates for a purely space-based time-delay interferometry setup with $r = L = 30$ AU have sensitivities of $\sqrt{fS_h} \sim 10^{-16}$ for $f = 10^{-6}\text{Hz}$, which corresponds to detecting variations of 0.3cm. It is conceivable that comparable distance control could be achieved from Earth since lunar laser ranging has achieved $< 0.1\text{cm}$ measurements of the Earth-Moon distance[60].

Previous Doppler tracking, which has been most successfully executed with the Cassini spacecraft, has been limited by mechanical variations in the analog path owing to e.g. thermal expansion or gravitational stresses. For Cassini, this resulted in centimeter-scale noise over relevant frequencies[59]. However, mechanical distortions could potentially be further reduced by using a smaller terrestrial radio dish constructed to be more rigid[59], by using an optical laser setup, or by employing a precise atomic clock on the spacecraft. More details on the latter two are provided below.

If mechanical noise can be significantly reduced, atmospheric delays are likely to become the limiting factor. The atmospheric delay that is most worrisome is the tropospheric "wet" delay from water vapor in the atmosphere because it is frequency independent – it cannot be removed by observing multiple frequencies. Although typical wet delays vary by several centimeters on day timescales towards zenith, much of this delay can be removed by precise atmospheric monitoring, such as with water vapor radiometers. Indeed, such monitoring occurred for the Cassini Doppler tracking system, for which[61] estimated its error by differencing the predictions of two identical systems. They predicted that the delay could be corrected to ~ 0.01 cm over times of hours to months, although their differencing methodology should be taken as a lower bound on the true error as it does not account for modeling uncertainties.

Figure 6 investigates the potential sensitivity of Doppler tracking of an $L = 10$ AU (left panel) and $L = 30$ AU (right panel) spacecraft. The solid blue curve is the strain sensitivity that a Doppler tracking arm could achieve if its sensitivity is set by spacecraft accelerations and the downlink radiometer noise with $C/N_0 = 60$ dB-Hz (left panel) and 40 dB-Hz (right panel) and broadcasting in the Ka band at $\lambda = 1$ cm, with these larger dB-Hz values than in previous plots reflecting that more collecting area can potentially be available for the Earth station. (The downlink is the limiting step in terms of phase noise.) Unlike in previous figures, where we assumed some geometric cancellation of the largely radial spacecraft acceleration, the radial nature of Doppler tracking to outer Solar System spacecraft means that nearly all of the acceleration projects onto the Earth-spacecraft chord. Still, mechanical noise and the atmosphere are likely to limit the sensitivity over this ideal curve. Indeed, the dotted blue points are the best constraints using Doppler tracking, achieved with the Cassini mission with $L \approx 10$ AU, with the sensitivity likely limited by mechanical noise[59]. Improvements in the Cassini noise by as much as several orders of magnitude would be required to reach the blue solid curve.
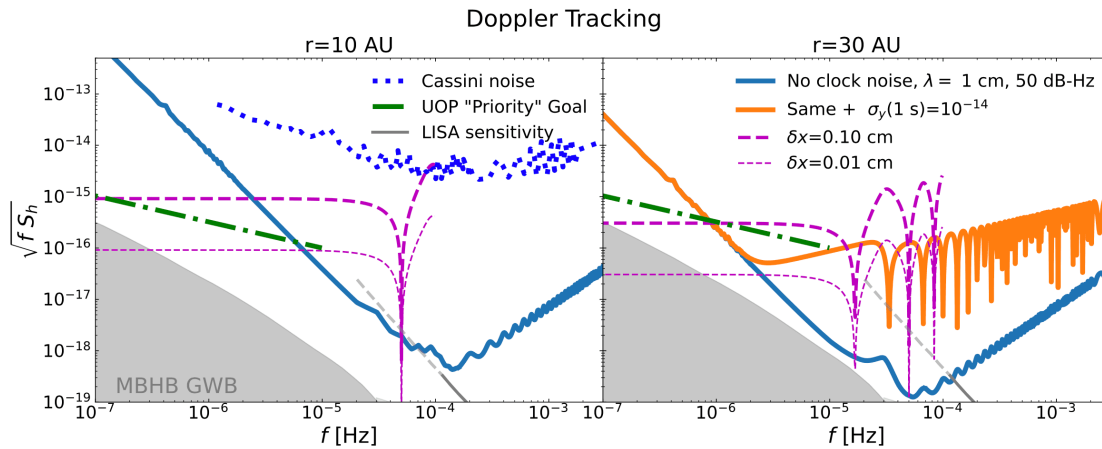
Figure 6. Gravitational wave strain sensitivities for the **third design architecture: the Doppler tracking concept**, sending $\lambda = 1$ cm radio signals between an Earth station and a $r = 10$ AU (left panel) and $r = 30$ AU (right panel) spacecraft. The solid blue curve is the strain sensitivity that an ideal instrument could achieve if its sensitivity is set by spacecraft accelerations and radiometer noise with the specified C/N_0. Mechanical noise and Earth's atmosphere likely limit the sensitivity over this ideal curve. The magenta dashed curves illustrate the noise power if the atmosphere and mechanical noise can be subtracted to a residual power that has equal variance per $\log f$ and equal to 0.1 cm and 0.01 cm, numbers motivated in the text. The orange Doppler-tracking sensitivity curve in the right panel is the same as the blue one except that it includes clock noise with $\sigma_y(1s) = 10^{-14}$. If the spacecraft is equipped with such a clock, an observable exists that can remove atmospheric and mechanical delays. The green dot-dashed curve shows the $f < 10^{-5}$ Hz 'priority' sensitivity goal for a future mission to Uranus of[23]. The dotted blue points in the left panel are the best constraints using Doppler tracking, achieved with the Cassini mission with $L \approx 10$ AU[59].

Atmospheric and mechanical delays could also be reduced by using a precise clock on the spacecraft and then doing one-way and two-way ranging ('One-way' uses the clock on the spacecraft as the phase reference that is differenced with a signal sent from Earth. 'Two-way' phases the spacecraft to the terrestrial phase and so does not require a precise clock on the spacecraft and, therefore, is the mode used by previous Doppler tracking experiments.) Analogous to time-delay interferometry, an observable can be constructed from the phases of the one-way and two-way ranging signals that cancels out any delays that occur at the time of emission and reception by the Earth station and does not remove all of the gravitational wave signal[62], namely by differencing the phases in this manner: $(\text{two-way}(t)) - (\text{one-way}(t)) - (\text{one-way}(t + L/c))$. The orange curve in Figure 6 is the same as the

blue curve but also includes clock noise with $\sigma_y(1s) = 10^{-14}$ – ten times lower $\sigma_y(1s)$ than the Deep Space Atomic clock.[10] (This type of observable also eliminates acceleration noise at one satellite. It could motivate a configuration with a more-resourced satellite in the high-acceleration near-Earth environment broadcasting to one in the outer Solar System or, alternatively, the satellite near Earth having a precise accelerometer and the acceleration noise nulled for the outer Solar System satellite.)

The magenta dashed curves shown at $f < 10^{-4}$ Hz show the residual noise power if the atmosphere and mechanical noise can be subtracted to a residual power that has an equal variance per $\log f$ (i.e. $1/f$ noise) and equal to 0.1 cm and 0.01 cm, numbers motivated above for the degree to which wet tropospheric delays could be cleaned. Although tropospheric delays have a redder spectrum than $1/f$, the spectrum[61] found after atmospheric correction was much closer to the $1/f$ form. These curves show that for $\lesssim 10^{-5.5}$ Hz, achieving $0.01 - 0.1$ cm error in mechanical and tropospheric delays would be sufficient to be limited by accelerations in the outer Solar System.[11]

There has been some recent interest in Doppler tracking for the μ Hz band in the context of a flagship Uranus mission[23]. The green dot-dashed curve in Figure 6 shows the $f < 10^{-5}$ Hz 'priority' sensitivity goal for this "Uranus Orbiter and Probe" (UOP) mission. This goal assumes an order of magnitude improvement of the theoretical Cassini noise, which was an order of magnitude better than what was actually achieved, and extrapolates this noise curve to lower frequencies. Our estimates show that at $f < 10^{-6}$ Hz, the accelerations on the spacecraft from variations in the solar irradiance and the solar wind must be corrected (likely by equipping the spacecraft with solar irradiance and plasma monitors) to achieve this sensitivity goal.

As discussed in[23] for the UOP, Doppler tracking using lasers might also be possible, but such an approach is unlikely to improve the sensitivity with respect to our radio estimates. Earth's turbulent atmosphere and the low C/N_0 downlink make phase locking in the optical impractical (as this requires both adaptive optics and a C/N_0 sufficient to achieve phase lock in the millisecond before the atmosphere changes). Thus, a laser Doppler tracking system would track the beat of laser pulses rather than the carrier phase. In contrast to timing the carrier phase – which allows a matched filter-like approach that results in the timing sensitivity scaling as L^{-1} –, the timing sensitivity for pulsed lasers scales as L^{-2}, which is problematic for the envisioned Solar System-scale baselines. Equation (13) in comparison to equation (12) shows that at $L = 30$ AU the timing noise for pulsed lasers will only be comparable with radio transmissions if a $D_2 \sim 10$ m telescope on Earth is deployed along with a $D_1 \sim 1$ m on the spacecraft. Additionally, optical transmissions experience a time-varying delay

from the atmosphere that is similar in magnitude to the wet tropospheric delay for radio waves: Near zenith, this delay is a couple of centimeters and can be corrected using atmospheric instrumentation similar to those used for the wet tropospheric delay. Attempts to correct for this error in the context of lunar laser ranging has resulted in millimeter-scale errors[63].

4. Instrumental considerations

At fixed strain noise power due to shot noise, the timing error, displacement error, and square of the angular pointing error are relaxed in proportion to the baseline distance. Thus, the extremely long arms of the presented concepts may reduce many design tolerances. Of course, long arms do come with the challenge that the transmitted signal strengths are much weaker compared to, e.g., LISA; Section 2.2 argued that the strengths are still sufficient to acquire stable phase locks. We now discuss other challenges of the laser and radio concepts, as well as challenges with placing spacecraft in the outer Solar System.

4.1. Laser design

Perhaps the biggest challenge in our laser-based concept is tuning the laser frequencies to cancel the relative velocities of the spacecraft. In all the scenarios we considered, the spacecraft would likely have much larger relative velocities compared to LISA, which are kept to $\lesssim 10$ m s^{-1}.[12] Relative velocities are problematic in that they spoil the cancellation of clock errors from time-delay interferometry, as the observed phase difference (eqn. 6) now has a strongly time-dependent phase given by $\phi_{\mathrm{het}} = 2\pi f_{\mathrm{het}} t$, where f_{het} is the part of the Doppler shift to the lasers emitted frequency that is uncorrected by any frequency tuning. This time-dependent phase means that, when it is recorded, the clock error t_{os} – or any timing error – again enters and results in a phase error of

$$\delta\phi_{\mathrm{het}} = 2\pi f_{\mathrm{het}} \delta t_{\mathrm{os}}. \tag{20}$$

For LISA, $\delta\phi_{\mathrm{het}}$ is large enough to substantially reduce instrument performance. The LISA design includes an elaborate scheme for correcting this error by superimposing weak pilot tones on top of the primary laser signal. The phase of these pilot tones contains the δt_{os} information that allows $\delta\phi_{\mathrm{het}}$ to be corrected and essentially eliminated from the phase noise. The low C/N_0 of the inter-spacecraft broadcasts in our concept likely makes this strategy of superimposing weaker pilot tones not viable.

Fortunately, our concept's much larger phase error tolerance may allow $\delta\phi_{\mathrm{het}}$ to be sufficiently small as to not dominate the error if the spacecraft adjoining both arms is equipped with an atomic clock. We

can write the standard deviation of $\tilde{\delta\phi}_{\mathrm{het}}$ in terms of the Allan deviation of its clock (cf. eqn. 2):

$$\tilde{\phi}_{\mathrm{het,rms}} = \frac{\sqrt{2\tau}(2\pi f_{\mathrm{het}})\sigma_y(\tau)}{(2\pi f)} = 0.1 \mathrm{\ rad\ Hz}^{-1/2} \left(\frac{\sigma_y(1s)}{10^{-13}}\right) \left(\frac{f_{\mathrm{het}}}{100 \mathrm{\ MHz}}\right) \left(\frac{f}{10^{-5} \mathrm{\ Hz}}\right)^{-1}. \quad (21)$$

For reference, the shot noise errors on the phase are 0.03 rad Hz$^{-1/2}$ for $[C/N_0]_{\mathrm{dB-Hz}} = 30$ dB–Hz (eqn. 10). We conclude that the heterodyne phase error is manageable with an atomic clock like the Deep Space Atomic Clock for which $\sigma_y(1s) \sim 10^{-13}$ if $f_{\mathrm{het}} \sim 10^2$ MHz, an order of magnitude higher than the maximum heterodyne frequency allowed for LISA.

The simplest orbits would send the spacecraft on radial trajectories with respect to the Sun. In this case, the relative velocities between the spacecraft could be tens of kilometers per second. A 10 km s^{-1} offset velocity would have to be compensated for by a ~ 0.3 Å shift of the output wavelength of a $\lambda = 10^4$ Å laser in order for it to interfere within the heterodyne specification. Tuneable lasers that can adjust their wavelength even to > 1 Å exist. Additionally, space interferometers like LISA must adjust the laser frequency on month timescales to compensate for this drift and stay under the maximum f_{het} that the system can tolerate[64][65]. For spacecraft on radial trajectories, the rate of change of the frequency from Doppler shifting between a spacecraft and some fixed reference is

$$\frac{df}{dt} = \frac{GM_\odot}{r^2\lambda} = 2 \times 10^9 \left(\frac{r}{30 \mathrm{\ AU}}\right)^{-2} \left(\frac{\lambda}{1000 \mathrm{\ Å}}\right)^{-1} \mathrm{\ GHz\ yr}^{-1}. \quad (22)$$

Equation (22) suggests that for radial trajectories and spacecraft at $r = 10 - 30$ AU, this tuning would also have to be done weekly or monthly to maintain a maximum heterodyne frequency of ~ 100 MHz.

A second challenge with lasers is controlling the phase noise from laser intensity variations, called 'relative intensity noise' (RIN), which scales inversely with received laser power, and the received power is exceptionally small owing to our concepts' long baselines. The square root of phase noise power spectrum from RIN is $\tilde{\phi}_{\mathrm{rms}}^{\mathrm{RIN}} \approx \sqrt{P_{\mathrm{local}}/(2\eta_{\mathrm{het}}P_{\mathrm{rec}})}r(f_{\mathrm{het}}) \times \chi$, where P_{local} is the power of the local laser that is being recombined with the received beam prior to phase readout and $r(f_{\mathrm{het}})$ is the RIN at the heterodyne frequency and $\chi < 1$ expresses how much of this term is canceled by 'balanced' detection methods that split the laser beams and combine their phase readout in a manner that, if perfectly performed, eliminates this dominant RIN term[35][66]. As RIN phase noise scales in the same manner with P_{rec} as the phase noise from shot noise, it is helpful to take the ratio with the analogous shot noise (eqns. 8 and 10):

$$\frac{\tilde{\phi}_{\mathrm{rms}}^{\mathrm{RIN}}}{\tilde{\phi}_{\mathrm{rms}}^{\mathrm{shot}}} = \sqrt{\frac{P_{\mathrm{local}}}{hc/\lambda}}r(f_{\mathrm{het}}) = 0.7\chi \left(\frac{P_{\mathrm{loc}}}{10^{-3} \mathrm{\ W}} \frac{\lambda}{1\mu m}\right)^{1/2} \left(\frac{r(f_{\mathrm{het}})}{10^{-8} \mathrm{\ Hz}^{-1/2}}\right), \quad (23)$$

where we have referenced the latter expression to the LISA requirement $r(f_{het}) \approx 10^{-8}$ Hz$^{-1/2}$ and a similar P_{local} as LISA.[13] Thus, especially for balanced detection that potentially could achieve $\chi < 0.1$ [67], RIN is likely not a limiting factor in the phase noise nor the phase lock if the lasers as long as the lasers achieve LISA-like specifications for $r(f_{het})$.

4.2. Radio design

There are many aspects that are easier for an experiment that relies on radio transmissions. For example, the requirements on any error that manifests as an apparent satellite displacement requirements are relaxed relative to laser transmissions by the factor of $\sim 10^4$ ratio of the wavelengths at frequencies where the sensitivity is set by radiometer noise. Additionally, relative velocities lead to much smaller frequency differences in the radio and, hence, much smaller timing errors in the phase (eqn. 20). Because the phase of the signal itself would be fed directly into the phase-lock loop for radio transmissions, in contrast to the laser setup in which the phase of the received laser is beat against a reference laser, relative intensity noise is not a concern. The pointing requirements are also relaxed relative to lasers, as lasers generate more planar wavefronts than radio dishes (which leads to larger phase errors from mispointing).

The radio design requires large dishes and an analog instrumental path via wires, such that thermal path length variations are likely to be larger than the optical design. For metals, the thermal expansion factor for 1 m of pathlength is typically $\sim 10^{-6} - 10^{-5}$ K^{-1}, with the smaller values for temperatures an order of magnitude below room temperature. To keep thermal expansion to 10^{-4} cm, as required for these pathlength changes to be a tenth or so of the radiometer noise on displacements (eqn. 11), the temperature should be controlled to just tens of Kelvin.

4.3. Outer Solar System considerations

One challenge to our proposal is that outer Solar System missions are significantly restricted when it comes to downlink data rates, to their mass, and to the power budget. Here we discuss each.

downlink data rates: Appendix C shows that, due to the low gravitational wave frequencies targeted, even 10 kbps hour-long downlinks every several months could be sufficient. Such downlink rates have been achieved to outer Solar System spacecraft, including New Horizons.

mass and orbits: The New Horizons spacecraft took nearly a decade to reach Pluto at 34 AU despite weighting just 500 kg[68]. However, with new Block 1B and Block 2 rockets from the Space Launch

System, plus advances in third/fourth stage boosters, it will soon be possible to launch several times more massive spacecraft at the same C3 velocity as New Horizons[69] and it is likely that similar specifications will be met by SpaceX and Blue Origin rockets. These new rockets would allow a spacecraft with the mass of New Horizons to reach Pluto in half the time. As achieving a particular orbit would require substantial fuel to slow down, the most feasible architecture would likely involve spacecraft that are continually drifting further from the Sun, possibly on unbound trajectories from the Solar System.[14]

power: Outer Solar System spacecraft must rely on radioisotope power. If the power output is similar to the radioisotope thermoelectic generator on the New Horizons spacecraft, the total power budget would be 250 Watt, and only a fraction of this could be dedicated to the spacecraft's science system. Meeting such a restrictive power budget seems potentially feasible given our result that $\sim 1 - 10$ Watt inter-spacecraft transmissions are sufficient. We further estimate similar power requirements for other systems, such as for compute and for the reaction wheels. For our designs that rely on an ultra-precise atomic clock, this technology likely would require substantial development. The Deep Space Atomic Clock requires 47 Watt[26], although there is a miniaturized version of this trapped ion clock that requires 6 Watt but has an order of magnitude larger Allan deviation[70]. Clocks based on optical frequency combs are being developed by NASA and likely can be smaller and less power-intensive, in addition to having smaller Allan deviations[71]. Power budgeting for our concepts is aided by removing the requirement of ultra-precise drag-free control – one of the most power-intensive systems on LISA.

4.4. Systematic checks and sky localization considerations

For gravitational wave observatories, there are two more important considerations to make when designing the mission - the ability to perform systematic checks, and the ability to localize gravitational wave signals on the sky. Systematic checks are necessary for being able to identify and differentiate occasional transient signals as being either instrumental in nature ("glitches") vs. being astrophysical in nature ("bursts"). And in general, sky localization to any source tends to be poorer for gravitational wave observatories as compared to electromagnetic observatories, since they are effectively all-sky antennae.

Considering terrestrial-based gravitational wave observatories, the duration of the signals they are sensitive to are short, typically of order seconds to minutes. During this time, the antenna pattern of

an individual interferometer observatory does not change a significant amount, therefore multiple observatories placed at very large separations across the Earth and in different orientations are necessary in order to estimate a sky location to any given signal. Having multiple observatories also benefits their systematic checking capabilities, as localized transient glitches in any one observatory would not appear across multiple, far-separated observatories. Astrophysical gravitational bursts would, however, appear correlated across all observatories. This helps give terrestrial observatories their glitch vetoing capabilities.

Considering the LISA mission, the duration of the signals they will be sensitive to are much longer, ranging between hours to years. During this time, the antenna pattern of the observatory will change as the constellation of satellites tumbles and orbits the Sun. The changing antenna pattern means that once an individual source has been identified, its localization will improve over time. The shorter the duration of the signal (e.g. for astrophysical bursts), the poorer the sky localization will be.

It is also anticipated that glitch vetoing will be partially enabled by having the three time-delay interferometry data channels, given the three arm design. Isolated transient instrumental noise signals occurring on one of the three spacecraft will propagate through the data channels differently than a common astrophysical burst that hits all three spacecraft. Therefore, in considering the three architectures presented in this work, these two factors may favor a multi-arm design. This fits with the two (or more) arm, time-delay interferometry architecture, or multiple concurrent instances of single arm missions, enabled either by atomic clocks or through Doppler tracking.

The angular resolution of an arm with length L we anticipate would be $\delta\theta \sim \lambda_{GW}/(L\text{SNR})$, with no rotational information around each arm and a $\pm\theta$ degeneracy, where SNR is the signal-to-noise of the gravitational wave event and this assumes that for $\lambda_{GW} \lesssim L$ the source drifts appreciably in frequency in order to select the correct 'interference fringe'. Since our concepts target extremely long wavelengths of $\lambda_{GW} = 2000(1\mu\text{Hz}/f)\text{AU}$, localizations $\delta\theta \lesssim 10°$ that would be most useful for electromagnetic follow-up will only be possible for bright sources that appear at the highest frequencies these concepts are potentially sensitivity (likely $f \gtrsim 10^{-4}\text{Hz}$). Furthermore, analogous to the LISA spacecraft, the spacecraft would likely drift by many AU over year timescales, reaching different points in the phase pattern of a long-term gravitational wave source, which could be further used for localization and to isolate gravitational wave signals from systematics.

5. Conclusions

This paper discussed the feasibility of detecting microhertz gravitational waves using outer Solar System spacecraft. This waveband probes the merger of supermassive black holes as well as a host of other gravitational wave phenomena. Taking advantage of the low acceleration environment beyond 10 AU, such a system could avoid the substantial technological development required for sufficient drag-free control at lower frequencies of $f < 2 \times 10^{-5}\,$Hz than the LISA mission targets. For solar distances as well as inter-spacecraft separations of ≥ 10 AU, we showed that the various interplanetary acceleration sources are small enough that even reaching a sensitivity where the noise is set by the stochastic gravitational wave background from massive black holes and white dwarf binaries appears achievable. We showed that such an acceleration-limited system would be easily able to detect the mergers of supermassive black holes at all likely redshifts.

We investigated systems that lock onto and time the phase from both laser and radio transmissions between the spacecraft. For both, we argued that even for 30 AU separations, transmission powers of ~ 10 Watt and reasonable mirror/dish sizes, stable phase locks may be achievable. We found for the laser concept this would require reduced frequency noise compared to the allowance for the LISA lasers, although possibly inline with the frequency noise achieved by the lasers in the GRACE-FO mission. Additionally, despite the much longer wavelengths of radio compared to laser transmissions, we showed that the sensitivity is likely to still be set by acceleration noise at $\lesssim 3 \times 10^{-4}$ Hz and, hence, independent of the wavelength of the transmissions. A system that uses the radio significantly reduces many design tolerances, such as those regarding pointing, transmission intensity variations, and spacecraft relative velocities. For radio implementations, interplanetary plasma contributes phase noise that can be effectively eliminated by transmitting at two wavelengths, with only a modest (factor of ~ 1.5) reduction in strain sensitivity and only when limited by radiometer noise.

This paper considered three possible architectures. The first was a two-arm (three-spacecraft) configuration that allows time-delay interferometry. This configuration was also the most sensitive without substantial improvement in space-certified atomic clocks. We considered configurations where the arms are at solar distances of 10 and 30 AU, and where the arm lengths were the same as the solar distance. Both configurations were able to detect merging $10^7 - 10^{10} M_\odot$ black holes out to substantial redshifts, and the 30 AU case was sensitive to middle-of-the-road predictions for the

stochastic gravitational background at $\sim 10^{-5}$ Hz. The sensitivity can be further improved by correcting for accelerations by monitoring solar irradiance variations and the solar wind.

The second architecture we considered involved just a single-arm. As a single arm cannot do interferometry to essentially eliminate clock noise, a single-arm design must incorporate a precise atomic clock on at least one spacecraft. We showed that the single-arm architecture equipped with a clock similar to the Deep Space Atomic Clock – a clock scoped for future interplanetary missions – could be sensitive to the characteristic strains of $10^8 M_\odot$ and $10^9 M_\odot$ supermassive black hole mergers, one of the most exciting signals anticipated in the microhertz waveband. Three orders of magnitude improvements in the timing precision over the Deep Space Atomic Clock, still far from the precision of the most precise terrestrial clocks, could achieve a sensitivity similar to the interferometric configuration when comparing at the same L.

The single-arm design becomes Doppler tracking of outer Solar System spacecraft when one of the nodes is located on Earth. Doppler tracking using outer Solar System spacecraft has a rich history[22]. Doppler tracking is the final architecture that we considered. We discussed the atmospheric and ground station delay requirements for Doppler tracking to reach interesting sensitivity benchmarks. We showed that for gravitational waves with $f \lesssim 1\mu$Hz, spacecraft accelerations must be corrected with on-board instrumentation for Doppler tracking to achieve the sensitivity goals of[23], envisioned in the context of a future Uranus probe. We also investigated the sensitivity of Doppler tracking if the spacecraft could be equipped with an atomic clock, allowing for a time-delay observable that nulls out atmospheric and some mechanical delays.

Placing spacecraft in the outer Solar System puts severe limits on the downlink rates, mass requirements, and power considerations. We showed that the achievable downlink rates should be sufficient because of the low frequencies of the targeted gravitational waves. We also argued that several tens of Watts of power could conceivably power the science systems on the spacecraft, within the realm of what can be supplied radioisotope thermoelectric generator. The mass of each spacecraft would likely have to be under 10^3kg in order to be launched to tens of astronomical units in $5 - 10$yr. The spacecraft requirement that we identified as potentially concerning (and in need of further study) is the severe restrictions on off-gassing (§ 2.3.6).

Although the discussion in this paper focused on concepts without acceleration control and μHz gravitational waves, some of our results could also apply to an outer Solar System concept that includes an ultra-precise accelerometer or that targets higher frequencies. The extremely long arms

of our hypothetical concepts mean that the accelerometer would not need to be as precise as in designs with shorter arms to reach the same sensitivity. Furthermore, the stable thermal and acceleration environment of the outer Solar System may facilitate acceleration control over the long periods of our targeted gravitational waves. Laser locks over $\sim 10\mathrm{AU}$ arms could allow better sky localizations at $f \lesssim 10^{-4}\mathrm{Hz}$ than more LISA-like concepts.

Statements and Declarations

Materials Availability

The code for the calculations presented in this work can be found at https://github.com/astromcquinn/GWwithDragFree.git.

Software

This work made use of the following software packages: Jupyter[72][73], matplotlib[74], numpy[75], and python[76]. Software citation information aggregated using The Software Citation Station[77].
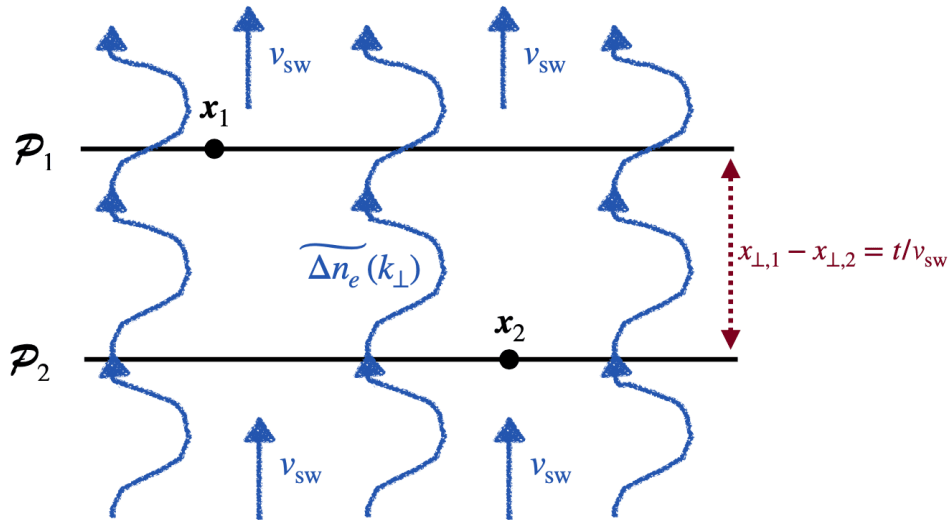
Appendix A. Dispersion

An issue with radio observations that is not present for our laser setup is that dispersion in the interplanetary plasma will contribute phase noise. Taking the density of the solar wind to be $n_e = 0.05(r/10\mathrm{AU})^{-2}\,\mathrm{cm}^{-3}$ (e.g., [47]), plasma dispersion leads to an error on the strain of

$$\delta h \sim c\kappa n_e = 2.6 \times 10^{-15}\left(\frac{r}{30\mathrm{AU}}\right)^{-2}\left(\frac{\lambda}{1\mathrm{cm}}\right)^2, \tag{A1}$$

where $\kappa = \lambda^2 e^2/(2\pi m_e c^3)$ converts an electron column density to a phase delay. Of course, the uniform solar wind signal does not look like gravitational waves. We can calculate the inhomogeneous part in terms of the power spectrum of the solar wind electrons, P_e, by first calculating the temporal

correlation function of the plasma delay between the two dishes. Additionally, because the solar wind acts to radially translate the inhomogeneities, the correlation function of delays between parallel paths can be related to the temporal correlation function that we desire. We approximate the paths along the arms as being at a fixed solar distance r and perpendicular to the direction of the Sun. We additionally assume that the perturbations along the path that the light travels do not change over the round-trip light-travel time for an arm, which means that our calculation will somewhat overestimate the effect for frequencies that satisfy $f \gtrsim c/(2L)$. Figure 7 illustrates the setup.

Figure 7. Illustration of the setup of the calculation presented in Appendixes A and B for the dispersive delays owing to the interplanetary plasma. Parallel paths $\mathcal{P}_1$ and $\mathcal{P}_2$ represent the arms linking two spacecraft at different times. We calculate the phase-delay correlation between these paths separated by $x_{\perp 1} - x_{\perp 2}$ and oriented perpendicular to the direction of the solar wind. We treat the solar wind as acting to translate inhomogeneities in the electron density with velocity v_{sw}, mapping spatial correlations between paths $\mathcal{P}_1$ and $\mathcal{P}_2$ to the desired temporal correlations. The spectrum of electron density fluctuations are represented by $\widetilde{\Delta n_e}(\mathbf{k})$, and only modes that have perpendicular orientations to the path contribute substantially to the correlations. One such nearly perpendicular mode of electron density fluctuations is illustrated.

The correlation of the phase delays between two parallel paths is

$$\langle \Delta \tau_{d,1} \Delta \tau_{d,2} \rangle = \kappa^2 \left\langle \int_{\mathcal{P}_1} dx_1 \Delta n_e(\mathbf{x}_1) \int_{\mathcal{P}_2} dx_2 \Delta n_e(\mathbf{x}_2) \right\rangle, \tag{A2}$$

where Δn_e is the 3D field of electron density fluctuations. Writing Δn_e in terms of its Fourier transform, the expectation value becomes

$$\langle \Delta\tau_{d,1}\Delta\tau_{d,2}\rangle = \kappa^2 \int_{\mathcal{P}_1} dx_1 \int_{\mathcal{P}_2} dx_2 \iint \frac{d^3\mathbf{k}_1 d^3\mathbf{k}_2}{(2\pi)^6} \langle \tilde{\Delta n_e}(\mathbf{k}_1)\tilde{\Delta n_e}(\mathbf{k}_2)^*\rangle e^{i(\mathbf{k}_1\cdot\mathbf{x}_1 - \mathbf{k}_2\cdot\mathbf{x}_2)}, \qquad (A3)$$

$$= \kappa^2 \int_{\mathcal{P}_1} dx_1 \int_{\mathcal{P}_2} dx_2 \int \frac{d^3\mathbf{k}}{(2\pi)^3} P_e(k) e^{i\mathbf{k}\cdot(\mathbf{x}_1-\mathbf{x}_2)}, \qquad (A4)$$

where we have defined the electron density power spectrum as $\langle \tilde{\Delta n_e}(\mathbf{k}_1)\tilde{\Delta n_e}(\mathbf{k}_2)^*\rangle = (2\pi)^3 P_e(k_1)\delta^D(\mathbf{k}_1 - \mathbf{k}_2)$. In the 'Limber approximation limit' that applies when the integral's support comes from $k \gg 2\pi/L$, the integral over the line–of–sight wavevector along $\mathcal{P}_1$ can be approximated as a δ–function. The δ–function can then be used to eliminate the integral over the wavevector along the path. The remaining integral along $\mathcal{P}_2$ evaluates to its length, L, such that equation (A4) reduces to

$$\langle \Delta\tau_{d,1}\Delta\tau_{d,2}\rangle \approx \kappa^2 L \int \frac{d^2\mathbf{k}_\perp}{(2\pi)^2} P_e(k) e^{i\mathbf{k}_\perp\cdot(\mathbf{x}_{\perp,1}-\mathbf{x}_{\perp,2})}, \qquad (A5)$$

where $\mathbf{x}_{\perp,1} - \mathbf{x}_{\perp,2}$ is the minimum separation between the two parallel paths.

The half–bandwidth temporal power of phase delay fluctuations is given by twice the temporal Fourier transform of $\langle \Delta\tau_{d,1}\Delta\tau_{d,2}\rangle$, using that time is related to position by $\mathbf{x}_{\perp,1} - \mathbf{x}_{\perp,2} = t/v_{sw}\hat{\mathbf{n}}$, where $\hat{\mathbf{n}}$ is the direction of the solar wind as well as the direction perpendicular to our two parallel paths. Thus,

$$P_{\Delta\tau_d}(f) = 2\int dt\, e^{-i\omega t} \langle \Delta\tau_{d,1}\Delta\tau_{d,2}\rangle = 2\kappa^2 L \int \frac{d^2\mathbf{k}_\perp}{(2\pi)^2} P_e(k)(2\pi)\delta^D(\omega - v_{w,\odot}\mathbf{k}_\perp\cdot\hat{\mathbf{n}}),$$

$$= \frac{2\kappa^2 L}{v_{w,\odot}} \int_{-\infty}^{\infty} \frac{dk_x}{(2\pi)} P_e\left(\sqrt{k_x^2 + \frac{\omega^2}{v_{sw}^2}}\right), \qquad (A6)$$

$$\approx 1.5\kappa^2 L \frac{v_{sw}}{\omega} P_e^{1D}(f,r), \qquad (A7)$$

where $f \equiv \omega/2\pi$ and k_x is the component of the wavevector perpendicular to the solar wind. Equation (A7) used that the 1D density power that is measured by, e.g., Voyager 2 is related to the 3D in the above expression by

$$P_e^{1D}(f) = \frac{2}{v_{sw,\odot}} \int_0^{\infty} \frac{dk}{(2\pi)} k P_e\left(\sqrt{k^2 + \frac{\omega^2}{v_{sw}^2}}\right), \qquad (A8)$$

where the factor of 2 is because this is the half bandwidth power. Since the integral that yields $P_e^{1D}(f)$ is somewhat different than that in equation (A6), to determine the numerical coefficient in

equation (A7) we assumed the scaling $P_e^{1D} \propto f^{-1.5}$ as motivated in § 2.3.2. However, we find this coefficient depends weakly on what power-law index is assumed over relevant indices.[15]

We can convert this to fluctuations in phase as

$$\tilde{\phi}_{\mathrm{disp,rms}} = \frac{c}{2\pi\lambda}\sqrt{4P_{\Delta\tau_d}(\omega)}, \tag{A9}$$

where the four is because the light travels out and back for each arm, probing essentially the same electron field for $f \lesssim c/(2L)$. At higher frequencies, the return path will see different electrons such that we should replace $4 \rightarrow 2$ – a correction which we ignore.

Converting the phase error to the error on the gravitational wave strain yields

$$\tilde{h}_{\mathrm{disp,rms}} = 4 \times 10^{-15}\,\mathrm{Hz}^{-1/2}R(f)^{-1/2}\left(\frac{L}{30\,\mathrm{AU}}\right)^{-1/2}\left(\frac{r}{30\,\mathrm{AU}}\right)^{-1.5}$$

$$\times \left(\frac{f}{10^{-5}\,\mathrm{Hz}}\right)^{-(\beta+1)/2}\left(\frac{P_{e,0}^{1D}}{10^{11.1}\,\mathrm{m}^{-6}\mathrm{Hz}^{-1}}\right)^{1/2}\left(\frac{\lambda}{1\,\mathrm{cm}}\right)^2, \tag{A10}$$

where we are using the form of the 1D solar wind density power given by equation (14), noting that $\beta \approx 2$ for $f < 10^{-5}\,\mathrm{Hz}$ (§ 2.3.2). We include the transfer function $R(f)$ to convert from the long wavelength limit (cf. eqn. 19).

Figure 8 shows the effect of dispersion for an interferometer operating at $\lambda = 1$cm. The dashed curves shows the strain noise power we estimate from plasma dispersion. The other curves are our predictions for the noise in the time-delay interferometry configuration once correcting for plasma dispersion by transmitting at two frequencies (see below; these are the same curves as in Fig. 4). The left panel shows $r = L = 10$AU, and the right panel $r = L = 30$AU assuming the spacecraft separation is nearly orthogonal to the radial direction so that the above calculations apply. Rather than assuming a power-law scaling as in equation (A10), the estimates in this figure use equations (A7) and (A9) as well as the 1D electron density power spectrum of the solar wind measured in [47] using Voyager 2 data.[16] This figure shows that the effect of dispersion is large and, if uncorrected, would limit the sensitivity of our concept at intermediate frequencies.
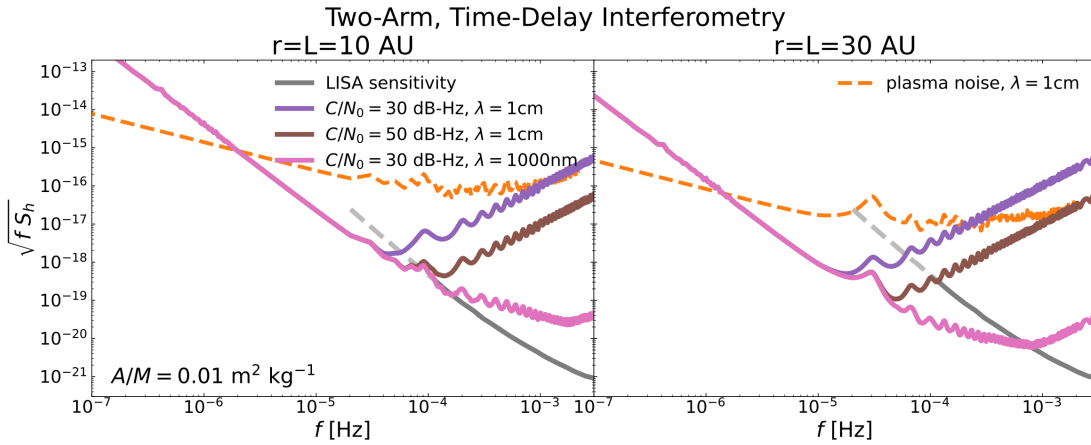
Figure 8. Effect of dispersion for an interferometer operating at $\lambda = 1$cm. The dashed curve shows the strain noise power we estimate from plasma dispersion. The other curves show the total noise once correcting for plasma dispersion with $\mathcal{A} = 1.5$ in the time-delay interferometer setup (the same curves as in Fig. 4). The left panel shows the case $r = L = 10$AU, and the right panel $r = L = 30$AU with the approximations discussed in § A. The estimates in this figure use equation (A9) and the electron density power spectrum of the solar wind measured by Voyager 2 [47].

While the phase noise due to the plasma can limit the sensitivity, it can be essentially eliminated by broadcasting at two wavelengths, λ_1 and λ_2, and then applying the following estimator for the inter-spacecraft displacement:

$$\hat{\Delta x} = \frac{\lambda_1 \lambda_2}{2\pi(\lambda_1^2 - \lambda_2^2)}(\lambda_1 \phi_2 - \lambda_2 \phi_1). \tag{A11}$$

Accelerations and gravitational waves lead to the same Δx as the previous single-phase estimator. Therefore, this estimator's gravitational wave strain sensitivity is not affected when accelerations set the noise. However, this estimator does come with the cost of an increased error when radiometer noise is important. When radiometer noise dominates, if we assume $\delta\phi_j \propto \lambda_j$ as applies if A_{eff} and T_{sys} are the same for the links at both λ_1 and λ_2, then phase errors are mapped to total errors as $\sigma_{\Delta x} = \sqrt{2}\lambda_1\lambda_2^2/(2\pi|\lambda_2^2 - \lambda_1^2|)\sigma_{\phi_1}$, using that $\sigma_{\phi_2} = \lambda_2/\lambda_1\sigma_{\phi_1}$, rather than $\sigma_{\Delta x} = \lambda_1/(2\pi)\sigma_{\phi_1}$ as for the single-phase estimator. Thus, it results in an increase in the estimator error by the factor $\sqrt{2}\lambda_2^2/|\lambda_2^2 - \lambda_1^2|$. If $\lambda_1 = 1$ cm and $\lambda_2 = 2$ cm ($\lambda_2 = 4$ cm), this results in an increase in the error of 1.8 (1.5) relative to what the error would be if we used the single phase estimator at λ_1. We parameterize the increase in noise power from de-dispersion relative to the (higher S/N) shortest

wavelength band by the factor $\mathcal{A}$ and include this in our error calculations, taking a fiducial value of $\mathcal{A} = 1.5$ (cf. eqn. 19).

Appendix B. Refraction and diffraction

Since Appendix A showed that dispersion (which scales as $\phi_{disp} \propto \lambda$) can be perfectly removed, the next question is how good of an assumption is it that $\phi_{disp} \propto \lambda$? For a homogeneous plasma, the correction to this long-wavelength scaling of the dispersion relation is suppressed by the ratio of the plasma frequency to the frequency squared. Since the plasma frequency for interplanetary gas is very small (~ 10 kHz) relative to the radio-wave frequencies of interest (~ 10 GHz), this correction to the $\phi_{disp} \propto \lambda$ scaling is extremely small.

A potentially larger effect is that the radio waves at different frequencies travel different paths owing to diffraction or refraction caused by the density inhomogeneities in the solar wind. Diffraction − or multipath propagation − results from phase fluctuations below the Fresnel scale $\sim \sqrt{\lambda L/(4\pi)}$. The Fresnel scale physically corresponds to the impact parameter that encapsulates most light paths that contribute constructively to the image. For the case at hand, the Fresnel scale corresponds to perturbations in the solar wind that pass the spacecraft with frequencies of $\omega_F \sim v_{sw}/\sqrt{\lambda L/(4\pi)} \sim 10(L/30AU \times \lambda/1cm)^{1/2}$Hz. We can use our estimate for the RMS phase fluctuations (eqn. A9) to evalauate the phase fluctuations at ω_F. Evaluating at the fiducial parameters where the parentheses in equation (A10) are unity, the phase fluctuations at $f_F \equiv \omega_F/(2\pi)$ are $f_F^{1/2}\tilde{\phi}_{disp,rms} \sim 10^{-7}$, and the leading-order contribution of diffraction to the RMS phase scales quadratically in $f_F^{1/2}\tilde{\phi}_{disp,rms}$ (as the linear order cancels since both positive and negative sub-Fresnel phase fluctuations contribute to the total). This suggests that the RMS diffractive phase fluctuations should have an absolutely negligible value of $\sim (f_F^{1/2}\tilde{\phi}_{disp,rms})^2 \sim 10^{-14}$. Furthermore, the sub-Fresnel fluctuations that drive the diffractive phase perturbations will decorrelate on timescales of ω_F^{-1}, leading to further suppression over this estimate. Thus, phase fluctuations from diffraction are likely to be extremely small.

Refraction is the displacement of images from a super-Fresnel density gradient. Refraction will contribute a larger effect since the phase perturbations in the solar wind are larger for $\omega \ll \omega_F$, and the longer wavenumbers of the participating modes mean there will be less decorrelation compared to diffraction. However, in the following, we show that refraction also sources a negligible amount of phase noise.

To analyze the effect of refraction, let us assume that all phase is acquired halfway between the two spacecraft in an arm, an assumption that will put an upper bound on refractive-phase fluctuations. The electric field's phase received at one receiver at wavelength λ is given by the Fresnel-Kirchhoff integral (e.g. [78])

$$\phi_\lambda = \arg\left(\frac{1}{2\pi i r_F^2}\int d^2\mathbf{x}\exp\left[i\frac{\mathbf{x}^2}{2r_F^2} + i\phi_d(\lambda_j, \mathbf{x})\right]\right). \tag{B12}$$

The integral is over the plane halfway between the two spacecraft, ϕ_d is the phase acquired by a sightline at position $\mathbf{x}$, and $r_F^2 \equiv \lambda L/(4\pi)$.

Since refraction owes to the smooth contribution from longer wavelengths than r_F, we can approximate the phase with a quadratic function given by $\phi_d(\mathbf{x}) \approx \phi_{d,l} + \nabla_i\phi_{d,l}x_i + \frac{1}{2}\nabla_i\nabla_j\phi_{d,l}x_ix_j$, where all the Taylor expansion coefficients are evaluated at $\mathbf{x} = 0$. Equation (B12) then evaluates to

$$\begin{aligned}
\phi_\lambda &\subset -\frac{r_F(\lambda)^2}{2}\left(\frac{\nabla_i\phi_{d,l}(\mathbf{x})}{1 + r_F(\lambda)^2\nabla_i^2\phi_{d,l}(\mathbf{x})}\right)^2, \\
&= -\frac{r_F(\lambda)^2}{2}|\nabla\phi_{d,l}(\mathbf{x})|^2 + \frac{r_F(\lambda)^4}{2}(\nabla_i\phi_{d,l}(\mathbf{x}))^2\nabla_i^2\phi_{d,l}(\mathbf{x}) + \ldots,
\end{aligned} \tag{B13}$$

where we have reconstituted the $\mathbf{x}$ argument for the coefficients in the expansion so that we can capture their time variability as the solar wind flows past, as well as omitted the wavelength argument in $\phi_d(\lambda_j, \mathbf{x})$ to simplify notation, and we have dropped an overall constant as this term is what was considered in Appendix A and is perfectly removed by the de-dispersion estimator given by equation (A11). We have rotated to the basis where $\nabla_i\nabla_j\phi_{d,l}(0)$ is diagonal, and i indices are implicitly summed. Equation (B13) shows that the leading refractive term is the square of the phase gradient times the Fresnel scale. Since each $r_F\nabla$ brings in a factor of f/f_F where $f_F \equiv \omega_F/(2\pi)$, the refractive effect should be suppressed at $f \sim 10^{-5}$ Hz and $\lambda = 1$ cm (noting that then $f/f_F \sim 10^{-6}$) by a factor of $\sim 10^{-13}$ relative to the mean dispersive term, which is $\propto \phi_{d,l}$ and whose effect was estimated in the previous section. This order-of-magnitude estimate uses that the phase fluctuation at $f = 10^{-5}$ Hz is ~ 0.1. This simple estimate is consistent with the following more detailed calculation.

To calculate the phase noise from refraction in more detail, let us consider the lowest-order non-constant term in equation (B13). Assuming the same setup as in Appendix A and illustrated in Figure 7, where temporal correlations can be related to spatial correlations of the advecting solar wind, we can calculate the corrections from refraction owing to phase correlations as

$$\langle \phi_\lambda(t)\phi_\lambda(t+\tau)\rangle \approx r_F(\lambda)^4 \left\langle |\nabla\phi_{d,l}(\mathbf{x})|^2 |\nabla\phi_{d,l}(\mathbf{x}+v_{sw}\tau\hat{\mathbf{n}})|^2 \right\rangle \tag{B14}$$
$$\subseteq 2r_F(\lambda)^4 \xi_{\nabla\phi}(\tau)^2,$$

where in addition to dropping an irrelevant constant, the last line assumed statistical isotropy and Gaussian statistics to express the four-point correlation function in terms of the two-point correlation function, where

$$\xi_{\nabla\phi}(\tau) = \langle \nabla\phi_{d,l}(\mathbf{x}) \cdot \nabla\phi_{d,l}(\mathbf{x}+v_{sw}\tau\hat{\mathbf{n}})\rangle.$$

The half-bandwidth power spectrum of phase fluctuations from refraction can be calculated from the Fourier transform of equation (B14):

$$P_{\phi,ref}(f=2\pi\omega) = 2r_F(\lambda)^4 \int dt\, e^{-i\omega t} \xi_{\nabla\phi}(t)^2 = 2r_F(\lambda)^4 \int \frac{d\omega'}{2\pi} P_{\nabla\phi}(\omega') P_{\nabla\phi}(\omega-\omega'), \tag{B15}$$

where the full-bandwidth power spectrum of $|\nabla\phi|$ is defined as

$$P_{\nabla\phi}(\omega) \equiv \int dt\, e^{-i\omega t} \xi_{\nabla\phi}(t) = \frac{(2\pi c)^2}{\lambda^2} \int dt\, e^{-i\omega t} \langle \nabla_i \Delta\tau_{d,1} \nabla_i \Delta\tau_{d,2}\rangle (v_{sw}t), \tag{B16}$$

and we have converted to gradients of the time delay rather than phase using that $\phi_d = 2\pi c/\lambda\tau_d$. Using the integral expression given by equation (A5) for $\langle\Delta\tau_{d,1}\Delta\tau_{d,2}\rangle$, and that the derivatives bring down factors of $\mathbf{k}_\perp$ under the integrand, we can write equation (B16) as

$$P_{\nabla\phi}(\omega) = \int dt\, e^{-i\omega t} \kappa'^2 L \int \frac{d^2\mathbf{k}_\perp}{(2\pi)^2} P_e(k) |\mathbf{k}_\perp|^2 e^{i\mathbf{k}_\perp \cdot \hat{\mathbf{n}} v_{sw} t}, \tag{B17}$$

$$= \frac{\kappa'^2 L}{v_{sw}} \int_{-\infty}^{\infty} \frac{dk_x}{(2\pi)} P_e\left(\sqrt{k_x^2 + \frac{\omega^2}{v_{sw}^2}}\right)\left(k_x^2 + \frac{\omega^2}{v_{sw}^2}\right), \tag{B18}$$

$$\approx \frac{4.4\kappa'^2 L|\omega|}{v_{sw}} P_e^{1D}(f,r), \tag{B19}$$

where $\kappa' = 2\pi c\kappa/\lambda$ and, similarly to how we reached equation (A7), we assumed a power-law for the electron density power spectrum. (The coefficient changes to 3.1 if $\beta = 2$ is taken for the spectral slope of the 1D power spectrum rather than $\beta = 1.5$, as was assumed to evaluate this expression.) The convolution that yields the phase noise power $P_{\phi,\mathrm{ref}}$ (eqn. B4) is only convergent for $3/2 < \beta < 2$, which conveniently is the rough range of indices favored by the Voyager 2 data, and has the scaling

$$P_{\phi,\mathrm{ref}}(f) \sim 10^2 \frac{r_F(\lambda)^4 \kappa'^4 L^2 f}{v_{sw}^2} \left[f P_e^{1D}(f,r)\right]^2 = 10^2 \frac{\pi^2 \kappa^4 L^4 f}{\lambda^2 v_{sw}^2} \left[f P_e^{1D}(f,r)\right]^2, \tag{B20}$$

where we have stuck in a 10^2 prefactor to match our order-of magnitude estimates from evaluating this integrand.

Finally, our expression for the RMS strain error using this estimate for $P_{\phi,\mathrm{ref}}$ and our de-dispersion estimator given in equation (A11) becomes

$$
\begin{aligned}
\tilde{h}_{\mathrm{ref,rms}} &= f(\lambda_1, \lambda_2) \frac{\lambda_1 \sqrt{4P_{\phi,\mathrm{ref}}(f)|_{\lambda_1}}}{2\pi L \sqrt{R(f)}}, \\
&\sim 10^{-25}\mathrm{Hz}^{-1/2} R(f)^{-1/2} \left(\frac{f(\lambda_1, \lambda_2)}{4}\right) \left(\frac{\lambda_1}{1\mathrm{cm}}\right)^4 \left(\frac{f}{10^{-5}\,\mathrm{Hz}}\right)^{(3-2\beta)/2}, \\
&\times \left(\frac{P_{e,0}^{1D}}{10^{11.1}\mathrm{m\ Hz}}\right) \left(\frac{r}{30\mathrm{AU}}\right)^{-3} \left(\frac{L}{30\mathrm{AU}}\right)^2.
\end{aligned}
\tag{B21}
$$

where $f(\lambda_1, \lambda_2) = \left| \frac{\lambda_2/\lambda_1^3}{(\lambda_1^2 - \lambda_2^2)} \left(\lambda_1 \lambda_2^3 - \lambda_2 \lambda_1^3\right) \right|$, which evaluates to $f(\lambda_1, \lambda_2) = 4$ if $\lambda_2 = 2\lambda_1$ and we have used the parameterization of the power given by equation (14). Equation (B21) shows that the effect of refraction is very small relative to other sources of noise.

Appendix C. Data rates

Due to the tens of astronomical units distances of the spacecraft in our concept, the concept developed here is likely constrained to a downlink data rate of ~ 10 kbps as has been achieved by previous outer Solar System missions such as the New Horizons spacecraft[68]. To estimate how much data would need to be telemetered back to Earth, let us compare the proposed mission with the LISA mission. LISA aims to send a downlink with a data rate of 230 kbps for eight hours every day[7]. Since LISA's goal is to constrain gravitational waves to frequencies as high as 1 Hz, it is designed to sample at 4 Hz[79][7]. Because LISA has three interferometric arms, the downlinked data include data streams from the six interferometric observables as well as from the positions of six test masses.

The proposed mission likely could accommodate a total data transmission that is a factor of $\sim 10^5$ smaller than LISA because (1) it targets $f < 10^{-4}$ Hz and so can sample on $10^4\times$ longer timescales, (2) it has one or two arms and no test masses, such that there are fewer data streams to downlink, and (3) it would have $\sim 10^4$ times less precision in the phase measurements relative to LISA and, hence, require fewer bits per sample. This much lower data rate means that an one-hour downlink at 10 kbps could potentially download an entire year of science data.

Footnotes

[1] The radio-dish design we propose to measure gravitational waves could plausibly also execute ~ 10 AU very long baseline interferometry to radio sources (particularly fast radio bursts) as has been

proposed for measuring cosmic distances and dark matter structure in [36] and [80]. Additionally, this concept may also be able to use the timing of Fast Radio Bursts repetitions to measure gravitational waves over frequencies similar to those considered here [81].

2 In practice, the arm lengths are not perfectly known, leading to a clock noise like equation (3) that does not cancel in the time-delay observable but where $L \to \delta L$, where δL is the uncertainty in the arm lengths [35]. This leads to the RMS strain error from clock noise being suppressed by the factor $\sim \delta L/L$ compared to in equation (4), where if the positions of the detectors are known to tens of centimeter precision, as is reasonable for ranging on Solar System scales [36], this leads to negligible error. Additionally, equation (6) is one example of a synthetic time-delay interferometry observable that can be constructed. More advanced combinations can be created that can, for example, further suppress the clock noise even when the arm lengths are changing during the measurement [82].

3 For the case $L_1 < L_2$ and in the long-wavelength limit $c/f \gg L_1$ the noise of this time-delay interferometry observable is increased by L_2/L_1 relative to what we would compute from the observable $\phi_1 - \phi_2$ without clock noise and if both arms have length L_2[83].

4 The low noise amplifiers can be further positioned on a cold plate on the spacecraft to achieve lower T_{sys}.

5 In contrast to LISA where this phase noise must be maintained to milliHertz frequencies to not compromise gravitational wave science, our concepts' $\sim 10^4 \times$ larger phase noise relaxes the allowance on S_f for $f \ll T_\phi^{-1}$ by this factor (for fixed spacecraft–spacecraft ranging error), which could provide more flexibility in material choices for the resonant cavity that stabilizes the lasers' frequencies[45].

6 We maintain the major features in the power spectrum using the data from Figure 12 in [46], but we omit much of the fine-grained structure in this power spectrum at $f > 10^{-5}$ Hz. Note that the effective area used for the conversion from irradiance to acceleration ($A_{\text{eff}} = 10 \, \text{m}^2$) would include the factor of two enhancement for a reflective surface directed at the Sun.

7 The power spectrum of the magnetic field is proportional to the accelerations from Lorentz forces, which is shown in Figure 2 (cf. § 2.3.4).

8 $R(f) \to 4/5 \sin^2(\gamma)$ at low frequencies, where γ is the angle between arms that we will take to be $90°$. This differs from the limit $R(f) \to 6/5$ that applies for LISA by the factor of $2 \sin^2(60°)/\sin^2(\gamma)$ owing

to LISA having two independent channels at low frequencies and 60° orientations for the arms [54]

9 To compute $R(f)$ for one arm, we drop the T_3 term in equation (23) in [53] that accounts for the cross-correlation of the gravitational wave signal between two arms, but include all other terms in their calculation of $R(f)$. This results in an $R(f)$ that is a factor of two larger than might be most natural to define for a single arm, but this extra factor of two cancels the two out front of equation (19) that owes to noise in both arms, allowing this equation to still apply for our one-arm concepts.)

10 For mechanical and other instrumental delays, the cancellation in the estimator of [62] occurs to the extent that the one-way and two-way ranging share the same analog path (even during transmit and receive). In our calculations, we have not used the correct transfer function of this observable, which we anticipate will result in a $\mathcal{O}(1)$ reduction in the sensitivity relative to the single-arm transfer function used for our calculation due to the cancellation of some of the gravitational strain terms in this combination.

11 Our estimates for noise of a Doppler tracking do not include the error from the Earth's ephemerides. Earth's position needs to be tracked and is uncertain at the ~ 100 m level, with these errors on year- and longer-timescales [84]. Ranging can be used to reduce this ephemerides error along the vector to the spacecraft, but this will come at the cost of being less sensitive to gravitational waves on the timescales for which the uncertainties ephemerides need to be fit for. Such fitting will bleed into shorter timescales than Earth's orbital period and possibly set the error for the lowest frequencies considered in our plots of $f \sim 10^{-7}$ Hz (as ~ 100 cm residuals will lead to larger errors than accelerations at such frequencies). A dedicated study is needed to understand the frequencies over which ephemerides errors limit the strain sensitivity.)

12 The way to avoid large relative velocities is if the outer Solar System spacecraft were in a circular orbit, each separated by 120° in orbital phase; [16][9]. Achieving such a configuration in the outer Solar System would be challenging.

13 Electronics noise can also add to the phase noise. We further find, using the online interface associated with Towards a Gravitational Wave Observatory Designer: Sensitivity Limits of Spaceborne Detectors[35], that a LISA-like $P_{local} = 2 \times 10^{-3}$ W minimizes the combination of shot, RIN and electronics noise for a system with $L = 30$ AU. Aside from L, these calculations assume LISA-like specifications for other system parameters. At this minimum, the shot noise of the received laser does indeed contribute most of the phase noise rather than RIN and electronics noise (and this interface

assumes no balanced detection such that $\chi = 1$). Additionally, for a much larger value of $f_{het} = 500$ MHz from $f_{het} = 25$ MHz that was used for the calculations just summarized, which increases electronics noise, we find the total noise from all three terms is minimized at $\sim 3\times$ shot noise alone when $P_{local} = 0.03$ Watt.

[14] Spacecraft trajectories that do not require achieving precise orbits may be an advantage over other interferometric concepts targeting microHertz gravitational waves, which require precise placement at $120°$ in orbital phase at $1 - 3$ AU[16][18][9][18].

[15] The coefficient changes from 1.5 to 1.6 if we use $P_e^{1D} \propto f^{-2}$, which may be more appropriate at $f \gtrsim 10^{-5}$ Hz.

[16] Since our derivation of equation (A7) assumed a power law, it is not rigorous to use the measured 1D electron density power spectrum, $P_e^{1D}(f)$: The different wavenumber weighting of the integrand over P_e that yields the measured 1D electron density spectrum (eqn. A8) and the phase noise delay power spectrum (eqn. A7) means that the features in the measured $P_e^{1D}(f)$ should be somewhat distorted in the phase noise.

References

1. ∧Abbott BP, et al. (2016). "Observation of Gravitational Waves from a Binary Black Hole Merger". Phys. Rev. Lett.. 116: 061102. doi:10.1103/PhysRevLett.116.061102.

2. ∧Abbott R, et al. (2023). "Physical Review X". Physical Review X. 13: 041039. doi:10.1103/PhysRevX.13.041039. 13, 041039.

3. ∧Abbott BP, et al. (2017). "Physical Review Letters". 119: 161101. doi:10.1103/PhysRevLett.119.161101. ADS.

4. a, bReardon DJ, et al. (2023). "Title not provided". Astrophysical Journal Letters. 951 (L6). doi:10.3847/2041-8213/acdd02. Link.

5. ∧Agazie G, et al. (2023). "The Astrophysical Journal Letters". The Astrophysical Journal Letters. 951: L8. doi:10.3847/2041-8213/acdac6.

6. ∧EPTA Collaboration et al. (2023). "A&A". Astronomy & Astrophysics. 678: A50. doi:10.1051/0004-6361/202346844. 678, A50.

7. a, b, c, d, e, fColpi M, et al. (2024). "arXiv e-prints". arXiv e-prints. doi:10.48550/arXiv.2402.07571. p. arXiv:2402.07571.

8. ∧*Arca Sedda M, et al. (2020). "Classical and Quantum Gravity". Classical and Quantum Gravity. 37: 2150 11. doi:10.1088/1361–6382/abb5c1. 37, 215011.*

9. a, b, c, d, e*Sesana A, et al. (2021). "Experimental Astronomy". Experimental Astronomy. doi:10.1007/s106 86–021–09709–9. 51, 1333.*

10. ∧*Neronov A, Roper Pol A, Caprini C, Semikoz D (2021). "Phys. Rev. D". 103: L041302. doi:10.1103/PhysRe vD.103.L041302.*

11. ∧*Bai Y, Chen T-K, Korwar M (2023). "Journal of High Energy Physics". Journal of High Energy Physics. doi:10.1007/JHEP12(2023)194. 2023, 194.*

12. ∧*Blas D, Jenkins AC (2022). "Title not provided". Physical Review Letters. 128: 101103. doi:10.1103/Phys RevLett.128.101103. ADS.*

13. ∧*Wang Y, Pardo K, Chang TC, Doré O (2022). "Physical Review D". 106: 084006. doi:10.1103/PhysRevD.1 06.084006. 106, 084006.*

14. ∧*Fedderke MA, Graham PW, Macintosh B, Rajendran S (2022). "". Physical Review D. 106: 023002. doi:1 0.1103/PhysRevD.106.023002. 106, 023002.*

15. ∧*Crosta M, Lattanzi MG, Le Poncin-Lafitte C, Gai M, Zhaoxiang Q, Vecchiato A (2024). "Scientific Repor ts". Scientific Reports. 14: 5074. doi:10.1038/s41598–024–55671–9.*

16. a, b, c, d*Folkner WM (2011). "A non-drag-free gravitational wave mission architecture". Technical repor t. https://pcos.gsfc.nasa.gov/studies/architecting/grav-wave/submissions/GWRFI-0003-Folkner.pdf.*

17. ∧*Ni W-T (2010). "Modern Physics Letters A". Modern Physics Letters A. doi:10.1142/S021773231000007 1. 25, 922.*

18. a, b, c, d*Martens W, Khan M, Bayle JB (2023). "Classical and Quantum Gravity". Classical and Quantum Gravity. 40: 195022. doi:10.1088/1361–6382/acf3c7. 40, 195022.*

19. ∧*Mueller G, et al. (2019). "In Bulletin of the American Astronomical Society". Bulletin of the American A stronomical Society. p. 243. doi:10.48550/arXiv.1907.11305. arXiv:1907.11305.*

20. a, b*Fedderke MA, Graham PW, Rajendran S (2022). "Physical Review D". 105: 103018. doi:10.1103/PhysR evD.105.103018. 105, 103018.*

21. a, b, c*McKenzie K, et al. (2011). "Technical report, LAGRANGE: A Space-Based Gravitational-Wave Detec tor with Geometric Suppression of Spacecraft Noise". Jet Propulsion Laboratory, California Institute of T echnology, Pasadena, California.*

22. a, b*Armstrong JW (2006). "Living Reviews in Relativity". Living Reviews in Relativity. 9: 1. doi:10.12942/ lrr-2006-1.*

23. <u>a</u>, <u>b</u>, <u>c</u>, <u>d</u>, <u>e</u>, <u>f</u>*Zwick L, et al. (2024). "arXiv e-prints". arXiv e-prints. doi:10.48550/arXiv.2406.02306. p. arXiv:2406.02306.*

24. <u>^</u>*Estabrook FB, Wahlquist HD (1975). "General Relativity and Gravitation". General Relativity and Gravitation. 6: 439. doi:10.1007/BF00762449. ADS.*

25. <u>^</u>*{IEEE Standards Association} (2009). IEEE Std Std 1139-2008. pp c1–35. doi:10.1109/IEEESTD.2008.4797525.*

26. <u>a</u>, <u>b</u>, <u>c</u>*Burt EA, et al. (2021). "Title not provided". Nature. 595: 43. doi:10.1038/s41586-021-03571-7. ADS.*

27. <u>^</u>*Wang D, Davydov VV, Rud VY (2021). "Journal of Physics: Conference Series". 2086: 012073. doi:10.1088/1742-6596/2086/1/012073.*

28. <u>a</u>, <u>b</u>*Oelker E, et al. (2019). "Nature Photonics". Nature Photonics. 13: 714. doi:10.1038/s41566-019-0493-4.*

29. <u>^</u>*Aeppli A, Kim K, Warfield W, Safronova MS, Ye J (2024). "Physical Review Letters". 133: 023401. doi:10.1103/PhysRevLett.133.023401. 133, 023401.*

30. <u>^</u>*Loeb A, Maoz D (2015). "arXiv e-prints". arXiv. doi:10.48550/arXiv.1501.00996. p. arXiv:1501.00996.*

31. <u>^</u>*Kolkowitz S, Pikovski I, Langellier N, Lukin MD, Walsworth RL, Ye J (2016). "Phys. Rev. D". 94: 124043. doi:10.1103/PhysRevD.94.124043.*

32. <u>^</u>*Faller JE, Bender PL, Hall JL, Hils D, Vincent MA (1985). In: Longdon N, Melita O, editors. ESA Special Publication. Vol. 226, Kilometric Optical Arrays in Space. pp. 157–163.*

33. <u>^</u>*Tinto M, Dhurandhar SV (2014). "Living Reviews in Relativity". Living Reviews in Relativity. 17: 6. doi:10.12942/lrr-2014-6.*

34. <u>a</u>, <u>b</u>, <u>c</u>, <u>d</u>*Misra P, Enge P (2012). Global positioning system: signals, measurements, and performance. Rev. 2nd ed. Lincoln, Mass.: Ganga-Jamuna Press.*

35. <u>a</u>, <u>b</u>, <u>c</u>, <u>d</u>*Barke S, Wang Y, Esteban Delgado JJ, Tröbs M, Heinzel G, Danzmann K (2015). "Classical and Quantum Gravity". Classical and Quantum Gravity. 32: 095004. doi:10.1088/0264-9381/32/9/095004.*

36. <u>a</u>, <u>b</u>, <u>c</u>, <u>d</u>*Boone K, McQuinn M (2023). "". ApJL. 947: L23. doi:10.3847/2041-8213/acc947. 947, L23.*

37. <u>^</u>*Njoku E, et al. (2014). SMAP Handbook. Jet Propulsion Laboratory, California Institute of Technology.*

38. <u>^</u>*Kardashev NS, Kovalev YY, Kellermann KI (2012). "The Radio Science Bulletin No 343". The Radio Science Bulletin. 343: 22. doi:10.48550/arXiv.1303.5200. 343, 22.*

39. <u>^</u>*High Frequency Electronics (2023). High Frequency Electronics.*

40. ∧*Barke S, et al. (2014). S2CID 106763425.*

41. a, b*Bachman B, et al. (2017). "Journal of Physics: Conference Series". Journal of Physics: Conference Series. 840: 012011. doi:10.1088/1742-6596/840/1/012011.*

42. ∧*Wang RT, Calhoun MD, Kirk A, Diener WA, Dick GJ, Tjoelker RL (2005). "In 2005 Joint IEEE International Frequency Control Symposium (FCS) and Precise Time and Time Interval (PTTI) Systems and Applications Meeting". Vancouver, British Columbia, Canada. https://ntrs.nasa.gov/search.jsp?R=20060044174.*

43. ∧*Taylor J. Deep Space Communications. Newark, UNITED STATES: John Wiley & Sons, Incorporated; 2016. Available from: http://ebookcentral.proquest.com/lib/washington/detail.action?docID=4648722.*

44. ∧*Ascheid G, Meyr H (1982). "IEEE Transactions on Communications". 30: 2228. doi:10.1109/TCOM.1982.1095423.*

45. a, b*Stacey J, Barwood G, Spampinato A, Tsoulos P, Robinson C, Gaynor P, Gill P (2023). In: Minoglou K, Karafolas N, Cugny B, editors. Proceedings of SPIE Vol. 12777, International Conference on Space Optics – ICSO 2022. SPIE. p. 127777F. doi:10.1117/12.2691441.*

46. a, b, c*Fröhlich C, Lean J (2004). "". Astronomy and Astrophysics Review. 12: 273. doi:10.1007/s00159-004-0024-1. 12, 273.*

47. a, b, c, d, e, f, g*Bellamy BR, Cairns IH, Smith CW (2005). "Journal of Geophysical Research: Space Physics". 110. doi:10.1029/2004JA010952.*

48. a, b*Smith E (1989). "Advances in Space Research". Advances in Space Research. 9: 159. doi:10.1016/0273-1177(89)90110-5.*

49. ∧*Grün E, Gustafson B, Mann I, Baguhl M, Morfill GE, Staubach P, Taylor A, Zook HA (1994). "". Astronomy & Astrophysics. 286: 915. Link.*

50. ∧*Grün E, Krüger H, Landgraf M (2000). In: Fitzsimmons A, Jewitt D, West RM, editors. Minor Bodies in the Outer Solar System. p. 99. doi:10.1007/10651968_13. arXiv:astro-ph/9902036.*

51. ∧*LAI ST. Fundamentals of Spacecraft Charging: Spacecraft Interactions with Space Plasmas. Princeton University Press; 2012. Available from: http://www.jstor.org/stable/j.ctvcm4j2n.*

52. ∧*Fedderke MA, Graham PW, Rajendran S (2021). "Physical Review D". 103: 103017. doi:10.1103/PhysRevD.103.103017. 103, 103017.*

53. a, b, c*Larson SL, Hiscock WA, Hellings RW (2000). "Phys. Rev. D". 62: 062001. doi:10.1103/PhysRevD.62.062001.*

54. a, b Robson T, Cornish NJ, Liu C (2019). "Classical and Quantum Gravity". *Classical and Quantum Gravity*. 36: 105011. doi:10.1088/1361-6382/ab1101. ADS.

55. ∧ Ajith P, et al. (2007). "Classical and Quantum Gravity". *Classical and Quantum Gravity*. doi:10.1088/0264-9381/24/19/S31. 24, S689.

56. a, b, c Cornish N, Robson T (2017). "In Journal of Physics Conference Series". IOP. p. 012024. doi:10.1088/1742-6596/840/1/012024. arXiv 1703.09858.

57. ∧ Nissanke S, Vallisneri M, Nelemans G, Prince TA (2012). "ApJ". 758: 131. doi:10.1088/0004-637X/758/2/131. 758, 131.

58. a, b, c Rosado PA (2011). "Phys. Rev. D". 84: 084004. doi:10.1103/PhysRevD.84.084004.

59. a, b, c, d, e Armstrong JW (2006). "Living Reviews in Relativity". *Living Reviews in Relativity*. 9: 1. doi:10.12942/lrr-2006-1.

60. ∧ Colmenares NR, Battat JBR, Gonzales DP, Murphy TW, Sabhlok S (2023). "". *Publications of the Astronomical Society of the Pacific*. 135: 104503. doi:10.1088/1538-3873/acf787. 135, 104503.

61. a, b Woo R, Guo WH (2004). "A New Technique for Determining the Strength of Interstellar Scintillation". Technical Report 158A. NASA Jet Propulsion Laboratory. https://tmo.jpl.nasa.gov/progress_report/42-158/158A.pdf.

62. a, b Armstrong JW (2021). "Gravitational Wave Search With the Clock Mission". https://ntrs.nasa.gov/citations/20210005049.

63. ∧ Marini JW, Murray CWM (1973). "Correction of Laser Range Tracking Data for Atmospheric Refraction at Elevations Above 10 Degrees". Technical Report NASA-TM-X-70555. NASA Goddard Space Flight Center. Available from: https://ntrs.nasa.gov/citations/19740007037.

64. ∧ Barke S. (2015). PhD thesis, Gottfried Wilhelm Leibniz Universität Hannover, Hannover, Germany. Available from: https://myaidrive.com/file-2T5njY8LayKGJLoBMyABpAhk.

65. ∧ Heinzel G, Álvarez-Vizoso J, Dovale-Álvarez M, Wiesner K (2024). "Phys. Rev. D". *Phys. Rev. D*. 110: 042002. doi:10.1103/PhysRevD.110.042002.

66. ∧ Wissel L, Wittchen A, Schwarze TS, Hewitson M, Heinzel G, Halloin H (2022). "Phys. Rev. Appl.". 17: 024025. doi:10.1103/PhysRevApplied.17.024025.

67. ∧ Wissel L, Hartwig O, Bayle J, Staab M, Fitzsimons E, Hewitson M, Heinzel G (2023). "Phys. Rev. Appl.". 20: 014016. doi:10.1103/PhysRevApplied.20.014016.

68. a, b Fountain GH, et al. (2008). "". *Space Science Reviews*. 140: 23. doi:10.1007/s11214-008-9374-8. ADS.

69. △NASA (2020). *Technical Report 20205007434, The Space Launch System for Science: A Launch Capability for the Next Decadal Survey and Beyond. Available from: https://ntrs.nasa.gov/api/citations/20205007434/downloads/SLS-PlanetaryDecadal-FINAL-LRP1%20091420.pdf.*

70. △Hoang TM, et al. (2023). *"Scientific Reports". 13: 10629. doi:10.1038/s41598-023-36411-x.*

71. △Tomio H, et al. (2024). *In: Navarro R, Jedamzik R, editors. Advances in Optical and Mechanical Technologies for Telescopes and Instrumentation VI. SPIE. p. 24. doi:10.1117/12.3020732.*

72. △Perez F, Granger BE (2007). *"Computing in Science and Engineering". Computing in Science and Engineering. 9: 21. doi:10.1109/MCSE.2007.53. Link.*

73. △Kluyver T, et al. (2016). *In ELPUB. pp 87–90.*

74. △Hunter JD (2007). *"Computing in Science & Engineering". Computing in Science & Engineering. 9: 90. doi:10.1109/MCSE.2007.55.*

75. △Harris CR, et al. (2020). *"Nature". Nature. 585: 357. doi:10.1038/s41586-020-2649-2.*

76. △Van Rossum G, Drake FL (2009). *Python 3 Reference Manual. CreateSpace, Scotts Valley, CA.*

77. △Wagg T, Broekgaarden FS (2024). *"arXiv e-prints". arXiv. p. arXiv:2406.04405.*

78. △Narayan R (1992). *"Philosophical Transactions of the Royal Society of London Series A". Philosophical Transactions of the Royal Society of London Series A. 341: 151. doi:10.1098/rsta.1992.0090. 341, 151.*

79. △Bayle J-B, Hartwig O (2023). *"Phys. Rev. D". 107: 083019. doi:10.1103/PhysRevD.107.083019.*

80. △Xiao H, Dai L, McQuinn M (2024). *"Physical Review D". 110: 023516. doi:10.1103/PhysRevD.110.023516. 110, 023516.*

81. △Lu Z, Wang L-T, Xiao H (2024). *"arXiv e-prints". arXiv e-prints. doi:10.48550/arXiv.2407.12920. p. arXiv:2407.12920.*

82. △Shaddock DA, Tinto M, Estabrook FB, Armstrong JW (2003). *"Phys. Rev. D". 68: 061303. doi:10.1103/PhysRevD.68.061303.*

83. △Larson SL, Hellings RW, Hiscock WA (2002). *"Phys. Rev. D". 66: 062001. doi:10.1103/PhysRevD.66.062001.*

84. △Vallisneri M, et al. (2020). *"Title not provided". ApJ. doi:10.3847/1538-4357/ab7b67. 893, 112.*

Declarations

Potential competing interests: No potential competing interests to declare.